



1     **A region-dependent seasonal forecasting framework for tropical cyclone genesis**  
2                                   **frequency in the western North Pacific**

3  
4  
5                                   Chao Wang<sup>1,2</sup>, Bin Wang<sup>2,1</sup> and Liguang Wu<sup>1</sup>

6                   <sup>1</sup> Key Laboratory of Meteorological Disaster of Ministry of Education, Joint  
7     International Research Laboratory of Climate and Environment Change, Collaborative  
8                   Innovation Center on Forecast and Evaluation of Meteorological Disasters,  
9                   Nanjing University of Information Science and Technology, Nanjing, China

10           <sup>2</sup> Department of Atmospheric Sciences and International Pacific Research Center,  
11                   University of Hawaii at Manoa, Honolulu Hawaii 96822, USA

12  
13  
14  
15  
16  
17  
18  
19  
20  
21  
22  
23

                                  August 17, 2019  
                                  Revised for Journal of Climate

Corresponding author:  
Bin Wang: [wangbin@hawaii.edu](mailto:wangbin@hawaii.edu)  
Chao Wang: [wangchao.typhoon@gmail.com](mailto:wangchao.typhoon@gmail.com)

## Abstract

It has been a common practice to predict total tropical cyclone (TC) genesis frequency over the entire western North Pacific (WNP). Here we show that TC genesis (TCG) exhibits distinct regional variability and sources of predictability. Therefore, we divide the WNP into four quadrants with 140°E and 17°N being dividing lines plus South China Sea (SCS) to predict five sub-regional as well as the entire WNP TCG frequency. Besides the well-known ENSO-induced seesaw relationship between the TCGs in the southeast and northwest quadrants, we found (a) an enhanced TCG in the northeast WNP is associated with a pronounced anomalous cyclonic circulation, which is maintained through its interaction with the underlying sea surface temperature (SST) anomalies; (b) an active TCG in the southwest WNP is accompanied by a zonally elongated positive vorticity anomaly and SST warming over the equatorial eastern Pacific; and (c) the SCS TCG is influenced by the upper-level South Asia High through modulating large-scale environmental parameters. Physically meaningful predictors are identified and a set of empirical prediction models for TCG frequency is established for each sub-region. Both the cross-validated reforecast for 1965-2000 and independent forecast for 2001-2016 show significant temporal correlation skills. Moreover, the sum of the predicted TCG frequency in five sub-regions yields a basin-wide TCG frequency prediction with a temporal correlation skill of 0.76 for the independent forecast period of 2001-2016. The results indicate its potential utility to improve the TC forecasting in the WNP.

## 1. Introduction

The WNP hosts about one-third of global named TCs per year (Gray 1968; Chan 2005) and experiences large year to year fluctuation in the total tropical storm days (Wang et al. 2010). Billions of people living in Pacific islands and Asian coastal regions are frequently subject to TC-induced disasters (Zhang et al. 2009; Peduzzi et al. 2012). Skillful seasonal prediction for TC activity would immensely benefit disaster mitigation (King et al. 2010). Therefore, achieving skillful seasonal forecasting products has been at the heart of TC research community since the 1970s (Nicholls 1979; Gray 1984; Chan et al. 1998; Camargo et al. 2007a, 2010; Zhan et al. 2012).

For the WNP, seasonal forecasting of TC activity was first attempted by the National Climate Center of China Meteorological Administration at the early 1990s (Zhan et al. 2012). Then, Chan et al. (1998) first issued seasonal forecasting products for the WNP by taking large-scale atmospheric and oceanic conditions into their statistical prediction model. Currently, various strategies including statistical method, coupled dynamic model and the so-called hybrid statistical-dynamical approach, have been used to make seasonal outlook for the WNP TC activity (Chan et al. 1998, 2001; Camargo et al. 2007a, 2010; Chen and Lin 2013; Zhan and Wang 2016; Zhang et al. 2016b). While the coupled dynamic models gradually show valuable prediction skill in recent decades (Chen and Lin 2013; Vecchi et al. 2014; Camp et al. 2015; Manganello et al. 2016), the statistical approach is still the principal way to issue TC seasonal forecast over the WNP (Chan et al. 1998, 2001; Camargo et al. 2007a, 2010; Fan and Wang 2009; Lu et al. 2010; Zhan et al. 2012; Zhan and Wang 2016; Kim et al. 2017; Zhang et al. 2018; Wang and Wang 2019).

Various factors have been used to predict the TCG frequency over the WNP,

including El Niño–Southern Oscillation (ENSO) (Chan et al. 1998, 2001; Wang and Chan 2002; Zhao 2016; Zhao and Wang 2016; Wang et al. 2019a,b; Zhao and Wang 2019), North Pacific Oscillation (Wang et al. 2007b; Chen et al. 2015; Zhang et al. 2018), Antarctic Oscillation (Ho et al. 2005; Wang and Fan 2007) and the Hadley circulation (Zhou and Cui 2008). More recently, the Pacific Meridional Mode (PMM, Zhang et al. 2016a, 2017), SST variations in the Indian ocean (Du et al. 2011; Zhan et al. 2011a; Tao et al. 2012), North Atlantic (Huo et al. 2015; Yu et al. 2015), and the SST gradient between the southwestern Pacific and the western Pacific warm pool (Zhou and Cui 2010; Zhan et al. 2013) have been suggested to be potential predictors for TCG frequency over the WNP. Recently, Wang and Wang (2019) found that the two leading modes of WNP subtropical high integrate the influences of the trans-basin SST variations, including North Indian Ocean (Zhan et al. 2011b; Du et al. 2011), North Pacific (Lander 1994; Wang and Chan 2002) and North Atlantic (Huo et al. 2015), on the WNP TC activity. Therefore, the WNP subtropical high can establish a unified framework for the seasonal forecasting of WNP TC activity (Wang and Wang 2019).

All of the aforementioned statistical prediction schemes usually take the basin-wide TCG frequency over the whole WNP as the targeted predictand. However, TCG over the WNP experiences distinct regional feature (Wang and Chan 2002; Kim et al. 2010) and the predictability sources of TCG in individual WNP sub-regions may differ from each other (Kim et al. 2009; Lu et al. 2010). Variations of the TCG frequency in individual sub-regions are usually not in phase, even anti-varied in some specific sub-regions (Figure not shown). In fact, even to the same climate factor, TCGs in different sub-regions respond differently due to the diverse responses in local large-scale conditions over the vast WNP (Wang and Chan 2002). The non-unified variation in sub-regions might make it difficult to predict the TCG frequency over the entire WNP

as a whole. In addition, TC disasters vary regionally (Pielke et al. 2008; Zhang et al. 2009; Peduzzi et al. 2012), thus the basin-wide TC activity metrics usually act as a poor indicator to those in sub-regions (Vecchi et al. 2014; Kossin 2017). The utility of these statistical forecasts would therefore be enhanced if seasonal TCG on scales finer than basin-wide could be skillfully predicted (Vecchi et al. 2014). Therefore, the primary objectives of this study are to investigate the predictability sources of regional TCG frequency, and further establish empirical models to predict the seasonal TCG frequency in individual sub-regions over the WNP.

In the next section, we describe the data and methods to establish and evaluate the prediction models. Section 3 explores the physical interpretation of TCG in individual sub-regions from the perspective of large-scale conditions. Section 4 presents the identified predictors for each of five sub-regions. The region-dependent seasonal forecasts and its predicting skill are shown in section 5 and a summary of the results and discussions are presented in section 6.

## **2. Data and method**

### **2.1 Data and definition of sub-regions**

TCG frequency is derived from the Joint Typhoon Warning Center (JTWC), which provides six-hourly records of positions (latitudes and longitudes) and maximum sustain wind speeds of TCs. TCs in this study are defined as tropical storms whose maximum wind speed reach or exceed  $17.2 \text{ m s}^{-1}$ . Monthly atmospheric data from the National Centers for Environmental Prediction (NCEP)-National Center for Atmospheric Research (NCAR) reanalysis (Kalnay et al. 1996) and SST from the Extended Reconstruction SST (ERSST) version 4 (Huang et al. 2015) are used to

interpret the impacts of large-scale conditions on TCG and identify the potential predictors.

The analysis period is from 1965 to 2016, and we focus on the peak season (July-September, Wang and Chan 2002, Wang and Wu 2012) of TCG over the WNP (0°-40°N, 100°E-180°). 1965 is taken as the starting year because satellite monitoring became routine around this year and TCs would be unlikely to be missed (Wang and Chan 2002; Chan 2006). The WNP is divided into five sub-regions (Fig.1), South China Sea (0°-25°N, 100°E-120°E), southwest WNP (0°-17°N, 120°E-140°E), northwest WNP (17°N-40°N, 120°E-140°E), southeast WNP (0°-17°N, 140°E-180°) and northwest WNP (17°N-40°N, 140°E-180°) following Wang and Chan (2002).

## 2.2 Methods to build and validate empirical models

Following Wang et al. (2015), correlation maps between the predictands (i.e., TCG frequency in five sub-regions during July-September) and anomalous large-scale conditions (SST, 2-m temperature, sea level pressure (SLP) and 850 hPa wind) prior to July are used to identify the potential predictors. Monthly/bi-monthly mean anomalies and tendency in large-scale conditions are taken as the potential predictive signals. Two types of predictors were used: (a) the persistent signals (represented by the seasonal mean) that indicate the slow variation of the lower boundary anomalies which will “persist” into the ensuing season, and (b) the tendency signals (represented by the difference in two months mean) that signify the tendency of following evolution. The potential predictive signals are identified as a potential predictor if there is a large-area of grid points where the correlation coefficient is significant at 95% confidence level (Lee et al. 2013; Yim et al. 2014; Wang et al. 2015b). After the above-mentioned two

steps, several identified physical meaningful predictors are considered as candidates. Then, stepwise regression, which can ascertain the relative independency of predictors and the best combination of the predictors, is used to build the empirical model for each sub-region. A 95% confidence level for Fisher's F test is used as the criterion to select predictors (Yim et al. 2014; Wang et al. 2015b). The lead-lag correlation between predictors and July-September mean large-scale circulation and environmental parameters are used to understand the cause-effect relationships between the predictors and predictand. Two validation methods, including cross-validated reforecast and independent forecast, are adopted to evaluate the prediction skills of empirical models (Wang et al. 2013; Yim et al. 2014). The cross-validated reforecast is obtained by first building the empirical model with samples excluding three years each time, and then use the derived empirical model to predict the TCG frequency for the three withheld years (Michaelson 1987). These processes are then repeated for all other years to obtain the cross-validated reforecast for 1965–2000. The independent forecast is then conducted for the rest 16-year period (2001–2016). Both the predictors selection and empirical model building is based on the samples during 1965–2000. The temporal correlation coefficient (TCC) and Mean Square Skill Score (MSSS) are used to measure the deterministic seasonal forecast skill (Murphy 1988). The MSSS compares the Mean Square Error (MSE) of the forecast to the MSE of climatology and thus reflects the forecast skill relative to the “forecasts” of climatology. Statistical significance of correlation is assessed using the two-tailed Student's t-test (Wilks 2006).

### **3. Physical interpretation of regional TCG frequency over the WNP**

Large-scale atmospheric and oceanic conditions play a crucial role in TCG over

the WNP (Gray 1968; Emanuel and Nolan 2004; Murakami and Wang 2010). In this section, we examine the anomalous large-scale circulation patterns and the corresponding boundary conditions concurring with the anomalous TCG frequency in individual sub-regions, which can help us gain insight into the physical linkage between the predictor and TCG frequency.

### 3.1 The northwest and southeast WNP

It has long been known that TCG in the northwest and southeast WNP is tightly linked to the ENSO phenomenon (Lander 1994; Wang and Chan 2002; Camargo et al. 2007b; Zhao et al. 2010; Wang and Wu 2016, 2018a). Generally, the favorable large-scale circulation pattern for TCG in the northwest and southeast WNP are consistent with previous studies (Figs. 2-3).

An active TCG in the northwest WNP is usually concurrent with a La Niña-like pattern in SST anomalies (Fig. 2a). The anomalous convective heating related to SST cooling over the equatorial central Pacific and SST warming over the Marine Continent can extend the subtropical high eastward through stimulating Rossby and Kelvin wave responses, respectively (Wang et al. 2013). The subtropical high ridge extends to the Philippines, generating cyclonic shear vorticity to its western flank (Fig. 2a) and favoring TCG in the northwest WNP. At the upper troposphere, the anomalous southeasterly in south China and northwesterly to its east generate strong upper-level divergence in the northwest WNP (Fig. 2b). The associated anomalous ascending motion is favorable for TCG (Wang and Chan 2002).

The large-scale circulations concurring with the active TCG in the southeast WNP are tightly linked to the developing phase of El Niño (Fig.3a). Specially, The



SST warming over the equatorial central-eastern Pacific can, through increasing convective heating, generate pronounced equatorial westerly anomalies in the western Pacific as Rossby response (Figs. 3a). The meridional shear vorticity of the anomalous westerly serves to favor TCG in the southeast WNP. At the upper troposphere, the anomalous anti-cyclone over the eastern WNP indicates the eastward migration in the tropical upper troposphere trough, which can favor the TCG in the southeast WNP by weakening vertical wind shear (Wu et al. 2015; Wang and Wu 2016, 2018b).

### 3.2 The northeast WNP

The favorable large-scale circulation patterns for TCG in the northeast WNP receive relatively less attention due to its weak impacts on Asian countries (Fig.1). Generally, active TCG in the northeast WNP are associated with anomalous ascending motion and cyclonic circulation, which are well-known to be favorable to TCG (Figs. 4a-b, Gray 1968). Actually, the anomalous cyclonic circulation is coupled to the underlying SST anomalies (Fig. 4a). On the one hand, the anomalous southwesterly to the south and southeast of cyclonic circulation superposed on the mean easterly trade wind, decreases total wind speed, suppresses sea surface evaporation and entrainment, and thus warms the SST in a southwest-northeast tilted band from tropical eastern WNP to the subtropical eastern Pacific. On the other hand, the anomalous southwesterly transport wet and warm air to the northeast of the anomalous cyclonic circulation. Both the SST warming and wet advection increase convective instability and serve to enhance the convection to the southeast of anomalous cyclonic circulation. The increased convective heating can then generate ascending Rossby waves, which in turn reinforces the anomalous cyclonic circulation (Wang et al. 2000, 2003, 2013; Xiang et

al. 2013). Meanwhile, the SST cooling induced negative convective heating over the equatorial eastern Pacific can stimulate an anomalous low-level anti-cyclone as Rossby wave response to its west. The southwesterly to the west flank of anomalous anti-cyclone can enhance the atmosphere-ocean feedback and then enhance the anomalous cyclonic circulation over the northeast WNP (Wang et al. 2000). Note that the Pacific SST distribution favoring TCG in the northeast WNP resembles that of PMM (Chiang and Vimont 2004), suggesting its impact on WNP TC activity comes mainly from the northeast WNP (Zhang et al. 2016a).

### 3.3 The southwest WNP

TCs formed in the southwest WNP exert great impacts on the Philippines and South Asia (Fig.1, Zhang et al. 2009). However, the favorable large-scale circulation patterns for TCG in this region are still unclear. Here enhanced TCG in the southwest WNP is associated with an anomalous cyclonic anomaly with convergence, which is located to the south of an anti-cyclonic circulation anomaly and connected to a strong cyclonic anomaly to its east (Fig. 5a). The corresponding 200 hPa winds show evident divergence (Fig. 5b). Moreover, the enhanced convective heating over the equatorial eastern Pacific can also contribute the cyclonic shear vorticity over the southwest WNP by generating anomalous equatorial westerlies (Figs. 5a). It should be noted that only the anomalous SST warming over the equatorial central-eastern Pacific can be treated as a forcing, while the SST underlying the two aforementioned anti-cyclonic circulations may just a result of atmospheric forcing (Figs. 5a-b, Wang et al. 2005). The different origin of the anomalous circulations indicates the possible importance of including the atmospheric forcing as predictors, which is usually missed in previous

studies (Zhan et al. 2013; Zhang et al. 2018).

### 3.4 The South China Sea

Although most TCs formed in the South China Sea (SCS) usually make landfall in South Asia, its variability sources are still unclear due to its weak relation to the local large-scale conditions (Wang et al. 2007a). Previous studies did not find significant correlation with the local thermodynamic conditions such as mid-level humidity and SST due to their sufficient climatological value in boreal summer; on the other hand, dynamic factors such as vorticity, large-scale vertical motion and vertical wind shear are found to play important roles in TCG in the SCS (Wang et al. 2007a). Here we found that these dynamic large-scale conditions are tightly linked to the variation in the upper-level South Asia high (SAH) (Fig. 6). In particular, a weak South Asia high is usually related to the suppressed vertical motion in Yangtze River valley, but enhanced convection in the SCS (Fig. 6a, Wu et al. 2007; Xuan et al. 2011; Wang et al. 2012; Yan et al. 2015) and thus favor the SCS TCG. Moreover, the anomalous upper-level westerly, which serves to weaken the climatological easterly wind shear, creates a favorable environment for TCG as well (Fig. 6a). At the lower troposphere, a cyclonic circulation is found to be concurrent with the enhanced TCG in the SCS (Fig. 6b). However, there is no significant local SST signal for TCG in the SCS (Fig. 6c), which is consistent with Wang et al. (2007a).

## 4. Physical predictors for individual sub-regions

The concurrent large-scale conditions with the active TCG can help us to find out the physically meaningful predictors for TCG in individual sub-regions. The

precursor (prior to July) which can contribute to those concurrent large-scale conditions are considered as potential predictors. Following this, the final predictors are identified by stepwise regression for TCG frequency in each of sub-region, some predictors are excluded due to their dependencies on the identified predictors (see section 2 for detail).

#### 4.1 The northwest and southeast WNP

For TCG frequency in the northwest WNP, two SST predictors are identified. The first one is a persistent predictor, NW-I, which features prominent La Nina-like SST cooling over the equatorial central Pacific during May-June in the active phase of TCG over the northwest WNP (Fig. 7a). Due to the phase locking feature of ENSO, the SST cooling can maintain to ensuing July-September. One may note that there is prominent SST warming in off-equatorial North Pacific as well, but it gradually dissipates during the La Nina development (Fig. 2a and Fig. 8a). The SST-cooling related decreasing Pacific zonal pressure gradient and the suppressed (enhanced) convection in the equatorial central-eastern Pacific (marine continent) serve to enhance the equatorial easterly and western North Pacific subtropical high (Fig. 8b, Wang et al. 2013; Xiang et al. 2013). The subtropical high ridge extends to the Philippines, generating cyclonic shear vorticity to its western flank (Fig. 8b). The cyclonic vorticity can increase the boundary layer Ekman convergence and then enhance the background vertical motion (Fig. 8c), favoring TCG in the northwest WNP (Wang and Chan 2002). The second predictor, NW-II, is an SST tendency predictor from September-October to May-June (Fig. 7b). Generally, there is a prominent SST cooling tendency over the north Indian ocean during the active period of TCG in the northwest WNP (Fig. 7b). The cooling tendency can persist to the following July-September and foreshadow an

enhanced Walker circulation and subtropical high via wind–evaporation–SST feedback (Figs. 8d-f). In a similar way, the anomalous subtropical high can enhance the TCG in the northwest WNP by generating cyclonic shear vorticity.

Two ENSO-related SST predictors are identified for the TCG frequency in the southeast WNP (Fig. 9). The first is a persistent predictor, SE-I, which shows prominent SST warming over the equatorial central Pacific during May-June in the active period of TCG in the southeast WNP. The anomalous SST warming can sustain to the following July-September due to the phase-locking characteristic of El Niño (Fig. 10a). The El Niño-related enhanced (suppressed) convection in the equatorial central-eastern Pacific (marine continent) shifts monsoon trough eastward, favoring the TCG in southeast WNP by increasing the background vertical motion and cyclonic vorticity (Fig. 10b, Wang and Chan 2002). In addition, at the upper-level, the tropical upper troposphere trough migrates to the east, weakening the westerly shear and therefore enhancing the TCG in the southeast WNP (Wu et al. 2015; Wang and Wu 2016, 2018b). The second predictor is the SST tendency from September-October to May-June over the equatorial central-Pacific (SE-II, Fig. 9b). The SST tendency can represent the direction of subsequent evolution of ENSO signal and thus indicate strength of El Niño and the migrations in large-scale circulations in ensuing July-September (Figs. 10d-f), which can greatly modify the TCG over the southwest WNP (Lander 1994; Chia and Ropelewski 2002; Wang and Chan 2002; Wang and Wu 2016, 2018b).

#### 4.2 The northeast WNP

Two predictors are identified for the TCG frequency in the northwest WNP. The first one is a persistent predictor, NE-I, which shows an SST dipole pattern with cooling

in the equatorial eastern Pacific and warming in subtropical North Pacific during the  
 active phase of TCG in the northeast WNP (Fig. 11a). Such a dipole pattern resembles  
 that of PMM, which can maintain to following months through air-sea interaction and  
 sustain an anomalous cyclonic circulation over the northeast WNP (Figs. 12a-c, Chiang  
 and Vimont 2004). On the one hand, the enhanced atmospheric heating in the  
 subtropical North Pacific can stimulate an anomalous cyclonic circulation to its west  
 and north as a Rossby wave response. On the other hand, the surface westerly and  
 southwesterly anomalies to the eastern flank of the anomalous cyclonic circulation can  
 reinforce the underlying SST warming by reducing total wind speed and sea surface  
 evaporation and entrainment cooling (Wang et al. 2000; Chiang and Vimont 2004;  
 Wang et al. 2013; Xiang et al. 2013). Meanwhile, the SST cooling induced negative  
 convective heating over the equatorial eastern Pacific can stimulate an anomalous low-  
 level anticyclone as a Rossby wave response to its west. The southwesterly to the west  
 flank of anomalous anti-cyclone can further enhance the atmosphere-ocean feedback  
 and then reinforce the anomalous cyclonic circulation over the northeast WNP (Wang  
 et al. 2000; Chiang and Vimont 2004). The anomalous circulation can further regulate  
 the TC formation in the northeast WNP by modifying the ambient low-level vorticity  
 and vertical wind shear (Zhang et al. 2016a). The second predictor, NE-II, is the 2m air  
 temperature tendency from September-October to May-June over the northwest Indian  
 ocean (Fig. 11b). The cooling tendency hints an SST cooling in the ensuing July-  
 September over the north Indian ocean (Fig. S1b). The SST cooling can further  
 stimulate a cold Kelvin wave propagating eastward to the WNP, decreasing the surface  
 pressure and leading to anomalous cyclonic circulation in the northeast WNP (Xie et al.  
 2009; Zhan et al. 2011b; Wang et al. 2013; Xie et al. 2016; Wang et al. 2017). The  
 opposite is true for an SST warming tendency over the northwest Indian ocean.

Therefore, a cooling (warming) tendency foreshadows an anomalous cyclonic (anti-cyclonic) circulation over the northeast WNP (Figs. 12d-f), which serves to enhance (suppress) TCG in the northeast WNP.

### 4.3 The southwest WNP

For the southwest WNP, two predictors are identified to predict the TCG frequency in this region (Fig. 13). The first one is the SLP tendency signal from November-December to May-June, SW-I, which is characterized by positive anomalies over the WNP in active years of TCG in the southwest WNP (Fig. 13a). The SLP tendency signal hints high pressures and anti-cyclonic circulations in the north WNP and north Australia in the ensuing July-September (Fig. 14a). The SLP tendency related circulation pattern in July-September is similar to that shown in Figure 5a, suggesting the possible utility of the SLP predictor in predicting TCG in the southwest WNP. The prominent easterly to the south flank of anti-cyclonic circulation can increase the cyclonic shear vorticity to its south (i.e., southwest WNP), which tends to favor TC development. Moreover, the two high-pressure zones to the north and south sides of the southwest WNP eventually constructed a relatively low-pressure zone over the southwest WNP, which can strengthen the low-level convergence and thus favor the TCG in this region (Figs. 14b-c). The second predictor is an SST persistent predictor, SW-II, which shows a warming over the equatorial eastern Pacific during May-June in the active phase of TCG in the southwest WNP (Fig. 13b). The SST warming can sustain to the ensuing July-September because of the phase-locking feature of ENSO. The SST warming induced atmospheric heating can emanate a cyclonic circulation pair symmetric about the equator as a Rossby wave response. The northern part of the

cyclonic pair extends to the southwest WNP and increases cyclonic vorticity in the southwest WNP (Figs. 14e-f). Meanwhile, meridional winds to the west edge of cyclonic circulation pair converge in the southwest WNP, which tends to enhance TCG in the southwest WNP as well.

#### 4.4 The South China Sea

Two predictors are identified for the TCG frequency over the South China Sea (Fig. 15). The first one is the June 850 hPa zonal wind over the tropical WNP, which features anomalous easterlies over Indonesia islands during active years of TCG in the South China Sea (Fig. 15a). In fact, the anomalous easterly suggests an inactive monsoon circulation in the South China Sea, which is usually corresponding to a weak South Asia High at the upper level (Liu and Zhu 2016). The persistent anomalous easterly in the ensuing July-September is consistent with the weakening of the South Asia High, which can favor TCG in the South China Sea by modifying vertical motion, the mid-level humidity and the low-level vorticity (Figs. 16b-c, Wu et al. 2007; Wang et al. 2007a, 2012; Yan et al. 2015). The second predictor is SST tendency from March-April to May-June over the eastern WNP (Fig. 15b). The warming tendency indicates an SST warming in the ensuing July-September. Such an SST warming is concurrent with an anomalous anti-cyclonic circulation extending from the eastern WNP to east Asia. The cyclonic shear vorticity to the south flank of the anomalous anti-cyclonic circulation creates a favorable environment for TCG in the SCS. Additionally, the cyclonic vorticity induced boundary layer Ekman convergence may enhance the ascending motion over the South China Sea as well (Figs. 16d-f).

Table 1 lists definitions of identified predictors for individual sub-regions. The



different predictors for individual sub-regions reflect the diverse predictability sources of TCG in individual sub-regions and further indicates the possible rationality of the region-dependent forecasting strategy.

## **5. Predictability and prediction skill for TC genesis in individual sub-regions**

### **5.1 Prediction**

The empirical models derived using the identified predictors listed in Table 1 can reasonably reproduce the inter-annual variability of TCG frequency in individual sub-regions. Particularly, the prediction (simulation) for TCG frequency in the northwest WNP, southeast WNP, northeast WNP, southwest WNP and South China Sea can achieve significant TCC skills of 0.65, 0.76, 0.62, 0.61 and 0.6, respectively, over the 52-year period of 1965-2016, suggesting about 40%-60% of the total variance of TCG frequency can be potentially predicted by using large-scale environmental parameters.

In order to examine the prediction skills of prediction models, a leave-three-out cross-validated reforecast is performed by taking 3 years out around the predicted year for 1965-2000, and independent forecasts are then made for the rest 16-year during 2001–2016. It is found that both of the cross-validated reforecast and independent forecast for TCG frequency are significantly correlated with observation in each of sub-regions (Fig. 17). For the northwest WNP, The TCC (MSSS) skill of cross-validated reforecast during 1965-2000 is 0.62 (0.22), and the independent forecast has significant TCC skill of 0.55 for the recent 16 years (2001–2016) (Fig. 17a). The prediction for the TCG frequency in southeast WNP exhibits the highest skill among the five sub-regions, whose TCC (MSSS) skills are 0.76 (0.36) for 1965-2000 reforecast and 0.68 (0.19) for

2001-2016 independent forecast (Fig. 17b). For the northeast WNP, TCC (MSSS) skill of the cross-validated reforecast during 1965-2000 is 0.58 (0.14), and independent forecast for 2001-2016 achieves a TCC (MSSS) skill of 0.55 (0.03). The TCC (MSSS) skills for the southwest WNP are 0.51 (0.14) for the cross-validated reforecast during 1965-2000 and 0.61(0.2) for the independent forecast in 2001-2016. The predicted TCG frequency in the South China Sea also shows valuable skill with TCC (MSSS) skills of 0.62 (0.22) for 1965-2000 reforecast and 0.61 (0.21) for 2001-2016 independent forecast (Fig. 17e).

The valuable skills in the predicted TCG frequency in individual sub-regions lend us confidence to further explore the predictability of basin-wide TCG frequency over the whole WNP. The predicted TCG frequency over the WNP is simply obtained by adding the predicted TC genesis frequency in all of five sub-regions (Fig. 17f). Actually, the predicted basin-wide TCG frequency also shows significant skills (Fig. 17f). For instance, TCC skill of the independent forecast for 2001-2016 achieves 0.76, which shows superior skill to that of traditional statistical approaches (Zhang et al. 2018). The superior prediction skills of the region-dependent strategy both in the basin-wide and regional scales, in fact, indicate its higher utility than the traditional predicting approaches, which can only provide us information about basin-wide TC activities.

## 5.2 Seasonal dependence of the prediction skill

One may curious that how long the prediction skills can last. Here we found that the favorable large-scale circulation pattern for TCG in each sub-region in July-September differs from that in the late season. Such differences are most evident in the SCS and the southwest WNP due to the salient changes in the seasonal/sub-seasonal

mean large-scale circulation pattern in these two sub-regions. For example, the SAH, which plays an important role in the SCS TCG in July-September, shifts southward to the Pacific Ocean in the late season and thus exerts relatively weak impact on the SCS TCG. Moreover, some SST predictors are highly coupled with atmosphere through wind-evaporation-SST (WES) feedback (Xie and Phlander 1994; Wang et al. 2000; Chiang and Vimont 2004; Wang et al. 2005), which is sensitive to mean circulation pattern. Accordingly, the WES feedback cannot work and maintain the anomalous circulation when seasonal mean circulation changed (Xie et al. 2016). In other words, the predicting skill highly depends on the seasonal mean large-scale circulation pattern. Figure 18 further shows the seasonal evolution of predicting skills in five sub-regions. For the SCS, meaningful skill can last to August-October. However, meaningful skill disappears in September-November due to the southward migration in the SAH. Meanwhile, the prediction skill for the southwest WNP experiences an abrupt breakdown in August-October, which attributes to the salient change in the favorable circulation pattern in October (Figure not shown). In contrast, the persistence of predicting skills in the northwest, southeast and northeast WNP are relatively longer. The longer-persistence in the northwest and southeast WNP can be attributed to the phase-locking feature of ENSO, which plays a vital role in the TCG frequency in the two sub-regions (Figs. 2-3). For the northeast WNP, two predictors are highly coupled with atmosphere thorough wind-evaporation feedback (Xie and Phlander 1994; Wang et al. 2000; Chiang and Vimont 2004). Therefore, the predicting skill gradually decreases as the retreat of summer monsoon. On the basin-wide scale, the prediction models can obtain a meaningful skill for July-October (Fig. 18). Table 2 shows the predicting results with target season of July-October. It can be seen that the results are generally similar to those in July-September except for the southwest WNP due to its

salient change in the favorable large-scale pattern in October. It means that the determinate factors for TCG in the southwest WNP are highly season-dependent, making it is difficult to predict the TCG in the southwest WNP for a long season.

## **6. Summary**

### **6.1 Conclusion**

Traditional statistical seasonal forecasting approaches for TC activity over the WNP take TCG frequency over the whole WNP as the targeted predictands. However, TCG over the WNP displays distinct regional features, and the basin-wide TC metrics usually act as a poor indicator to those in WNP sub-regions. The utility of the forecast products would, therefore, be enhanced if seasonal TC activity on scales finer than basin-wide could be skillfully predicted (Vecchi et al. 2014). This motivates us to establish a regional-dependent seasonal forecasting framework for TCG frequency over the WNP.

We have identified the large-scale circulation patterns and underlying boundary conditions cooccurring with active TCG in individual sub-regions. Besides the well-known ENSO-related seesaw relationship between the TCG frequency over the southeast and northwest WNP, we find that the enhanced TCG in the northeast WNP is associated with a pronounced cyclonic circulation anomaly, which is maintained through interaction between the cyclonic circulation and the underlying tri-pole SST anomalies in the northern Indo-Pacific. The anomalous cyclonic circulation can favor the TCG by modifying ambient low-level vorticity and vertical wind shear. For the southwest WNP, the favorable circulations and boundary conditions for TCG are the two high pressures to the two sides of the southwest WNP and the SST warming over

the equatorial central-eastern Pacific. The high-pressure associated circulations and the SST warming-related anomalous equatorial westerly can generate cyclonic vorticity and enhance the convergence in the southwest WNP, and thus favor the TCG. For the South China Sea, we found that a weak South Asia High can contribute to the active TCG by enhancing the vertical motion and weakening the climatological easterly wind shear in the northern South China Sea.

Based on the simultaneous large-scale circulation and boundary conditions, the precursors that can contribute to those concurrent large-scale conditions are considered as potential predictors. Several physically meaning predictors are identified for each sub-region. We found that ENSO precursors to predict TCG frequency over the northwest and southeast WNP, while the May-June mean dipole SST pattern which resembles PMM and 2-m temperature tendency over the west Indian ocean are found to be useful to predict TCG frequency in the northeast WNP. Seasonal prediction for TCG frequency in the southwest WNP and the South China Sea usually shows limited skills. Here we found the SLP tendency over the northern WNP and SST over the equatorial central-eastern Pacific can provide predictive information for TCG in the southwest WNP. For TCG in the South China Sea, the June 850 hPa wind over the Indonesia and SST tendency over the eastern WNP can provide useful precursors. The possible causative linkages between identified predictors and predictands are also discussed.

To investigate the predictability of TCG frequency in individual sub-regions, a set of empirical prediction models are established using the aforementioned predictors. It is found that the physical-empirical models can reasonably reproduce the inter-annual variability of TCG frequency in each of five sub-regions. Particularly, the prediction (simulation) for TCG frequency in the northwest WNP, southeast WNP, northeast WNP,

southwest WNP and South China Sea can achieve significant TCC skills of 0.65, 0.76, 0.62, 0.61 and 0.6, respectively, over the 52-year period of 1965-2016. Moreover, we used data from 1965-2000 as a training period to build prediction equation and performed a 16-year independent prediction. The independent reforecast for TCG frequency during 2001-2016 over the northwest WNP, southeast WNP, northeast WNP, southwest WNP and the South China Sea achieves significant TCC skill of 0.55, 0.68, 0.55, 0.61, 0.61, respectively. Surprisingly, their sum (i.e. the predicted TCG frequency for the whole WNP) also demonstrates superior predicting skill with a TCC skill of 0.76 for the independent forecast period of 2001-2016. The superior skills both in the basin-wide and regional scales of the region-dependent strategy indicate its higher utility comparing to the traditional statistical prediction approach, which only provides us with TC information for the whole basin.

## 6.2 Discussion

TCG in the vast WNP experiences distinct regional features (Wang and Chan 2002; Kim et al. 2010), and it does not experience unified variations even in response to the same large-scale forcing. The distinct regional characteristic in TCG over the WNP should be considered when establishing prediction models. The proposed region-dependent forecasting strategy can be an effective pathway to yield higher skill and utility than the traditional statistical prediction approaches.

Although valuable prediction skills in the basin-wide and regional TCG frequency are found in the region-dependent forecasting strategy, some limitations exist in this approach. The first is the possible nonstationary relationship between the predictor and predictand, which is a common limitation for empirical prediction method.

For instance, the relation between the PMM and TCG frequency in the northeast WNP weakens in the recent two decades, making the prediction skill comparatively low in the independent forecast during 2000-2016 (Figure is not shown). Moreover, The TCC skill for the TCG in the WNP during 1965-2000 relatively weaker than each sub-region, but it shows better skill than those in sub-regions for 2001-2016. It means the predicting errors in each subregion may be accumulated during 1965-2000 but offset each other during 2001-2016. This result indicates an unstable relationship of predicting errors in individual may play a role in predicting skills. Second, the proposed physical linkages between the predictors and predictands are largely based on physical reasoning. While the involved physical processes how the selected predictors affect TCG in the southeast and northwest WNP have been well-established by previous studies, how the selected predictors influence TCG in northeast and southwest WNP and the South China Sea still requires more work to examine the detailed physical processes. Numerical models provide us with a promising pathway to resolve these issues. Additionally, definitions of sub-regions are originally designed to understand the ENSO impacts on TCG over the WNP (Wang and Chan 2002), which may not be best suitable for representing the regional features of TCG on the inter-annual time scale. The predictable mode analysis may be a more viable strategy to portraying this regional features as used in Wang et al. (2015a), and we intend to explore this issue in a future study.

**Acknowledgements.** This study was jointly supported by the National Natural Science Foundation of China (Grant No. 41705060, 41420104002, 41730961 and 41675072), the Natural Science Foundation of Jiangsu Province (BK20170941) and the National Key Research and Development Program of China (Grant No. 2016YFA0600401). This is the NUIST-Earth System Modeling Center (ESMC) publication number XXX,

the School of Ocean and Earth Science and Technology (SOEST) publication number XXXX, and the IPRC publication number YYYY.

## References:

Camargo, S. J., A. G. Barnston, P. J. Klotzbach, and C. W. Landsea, 2007a: Seasonal tropical cyclone forecasts. *WMO Bull.*, **56**, 297–309.

———, K. A. Emanuel, and A. H. Sobel, 2007b: Use of a genesis potential index to diagnose ENSO effects on tropical cyclone genesis. *J. Clim.*, **20**, 4819–4834, <https://doi.org/10.1175/JCLI4282.1>.

———, A. H. Sobel, A. G. Barnston, and P. J. Klotzbach, 2010: The Influence of Natural Climate Variability on Tropical Cyclones, and Seasonal Forecasts of Tropical Cyclone Activity. *Global Perspectives on Tropical Cyclones*, C. Johnny C L and K. Jeffrey D, Eds., World Scientific, 325–360.

Camp, J., M. Roberts, C. Maclachlan, E. Wallace, L. Hermanson, A. Brookshaw, A. Arribas, and A. A. Scaife, 2015: Seasonal forecasting of tropical storms using the Met Office GloSea5 seasonal forecast system. *Q. J. R. Meteorol. Soc.*, **141**, 2206–2219, <https://doi.org/10.1002/qj.2516>.

Chan, J. C., 2006: Comment on “Changes in tropical cyclone number, duration, and intensity in a warming environment.” *Science* (80-. ), **311**, 1713; author reply 1713, <https://doi.org/10.1126/science.1121522>.

Chan, J. C. L., 2005: Interannual and interdecadal variations of tropical cyclone activity over the western North Pacific. *Meteorol. Atmos. Phys.*, **89**, 143–152, <https://doi.org/10.1007/s00703-005-0126-y>.



- 583 Chan, J. C. L., J. Shi, and C.-M. Lam, 1998: Seasonal Forecasting of Tropical  
584 Cyclone Activity over the Western North Pacific and the South China Sea.  
585 *Weather Forecast.*, **13**, 997–1004, [https://doi.org/10.1175/1520-](https://doi.org/10.1175/1520-0434(1998)013<0997:SFOTCA>2.0.CO;2)  
586 0434(1998)013<0997:SFOTCA>2.0.CO;2.
- 587 ———, J.-E. Shi, and K. S. Liu, 2001: Improvements in the Seasonal Forecasting of  
588 Tropical Cyclone Activity over the Western North Pacific. *Weather Forecast.*,  
589 **16**, 491–498, [https://doi.org/10.1175/1520-](https://doi.org/10.1175/1520-0434(2001)016<0491:IITSFO>2.0.CO;2)  
590 0434(2001)016<0491:IITSFO>2.0.CO;2.
- 591 Chen, D., H. Wang, J. Liu, and G. Li, 2015: Why the spring North Pacific Oscillation  
592 is a predictor of typhoon activity over the Western North Pacific. *Int. J.*  
593 *Climatol.*, **35**, 3353–3361, <https://doi.org/10.1002/joc.4213>.
- 594 Chen, J.-H., and S.-J. Lin, 2013: Seasonal Predictions of Tropical Cyclones Using a  
595 25-km-Resolution General Circulation Model. *J. Clim.*, **26**, 380–398,  
596 <https://doi.org/10.1175/JCLI-D-12-00061.1>.
- 597 Chia, H. H., and C. F. Ropelewski, 2002: The interannual variability in the genesis  
598 location of tropical cyclones in the northwest Pacific. *J. Clim.*, **15**, 2934–2944.
- 599 Chiang, J. C. H., and D. J. Vimont, 2004: Analogous Pacific and Atlantic Meridional  
600 Modes of Tropical Atmosphere – Ocean Variability. *J. Clim.*, **17**, 4143–4158,  
601 <https://doi.org/10.1175/JCLI4953.1>.
- 602 Du, Y., L. Yang, and S.-P. Xie, 2011: Tropical Indian Ocean Influence on Northwest  
603 Pacific Tropical Cyclones in Summer following Strong El Niño\*. *J. Clim.*, **24**,  
604 315–322, <https://doi.org/10.1175/2010JCLI3890.1>.
- 605 Emanuel, K. A., and D. S. Nolan, 2004: Tropical cyclone activity and the global

climate system. *Preprints, 26th Conf. on Hurricanes and Tropical Meteorology*,  
*Miami, FL, Amer. Meteor. Soc. A*, Vol. 10 of.

Fan, K., and H. Wang, 2009: A New Approach to Forecasting Typhoon Frequency  
over the Western North Pacific. *Weather Forecast.*, **24**, 974–986,  
<https://doi.org/10.1175/2009WAF2222194.1>.

Gray, W. M., 1968: Global view of the origin of tropical disturbances and storms.  
*Mon. Weather Rev.*, **96**, 669–700.

———, 1984: Atlantic seasonal hurricane frequency. Part I: El Nino and 30 mb quasi-  
biennial oscillation influences. *Mon. Weather Rev.*, **112**, 1649–1668.

Ho, C.-H., J. Kim, H. Kim, C. Sui, and D. Gong, 2005: Possible influence of the  
Antarctic Oscillation on tropical cyclone activity in the western North Pacific. *J.*  
*Geophys. Res.*, **110**, D19104, <https://doi.org/10.1029/2005jd005766>.

Huang, B., and Coauthors, 2015: Extended reconstructed sea surface temperature  
version 4 (ERSST.v4). Part I: Upgrades and intercomparisons. *J. Clim.*, **28**, 911–  
930, <https://doi.org/10.1175/JCLI-D-14-00006.1>.

Huo, L., P. Guo, S. N. Hameed, and D. Jin, 2015: The role of tropical Atlantic SST  
anomalies in modulating western North Pacific tropical cyclone genesis.  
*Geophys. Res. Lett.*, **42**, 2378–2384, <https://doi.org/10.1002/2015GL063184>.

Kalnay, E., and Coauthors, 1996: The NCEP/NCAR 40-year reanalysis project. *Bull.*  
*Am. Meteorol. Soc.*, **77**, 437–471.

Kim, H.-S., C.-H. Ho, P.-S. Chu, and J.-H. Kim, 2009: Seasonal prediction of  
summertime tropical cyclone activity over the East China Sea using the least  
absolute deviation regression and the Poisson regression. *Int. J. Climatol.*, **30**,

629 n/a-n/a, <https://doi.org/10.1002/joc.1878>.

630 Kim, J.-H., C.-H. Ho, and P.-S. Chu, 2010: Dipolar redistribution of summertime  
631 tropical cyclone genesis between the Philippine Sea and the northern South  
632 China Sea and its possible mechanisms. *J. Geophys. Res.*, **115**,  
633 <https://doi.org/10.1029/2009jd012196>.

634 Kim, O.-Y., H.-M. Kim, M.-I. Lee, and Y.-M. Min, 2017: Dynamical–statistical  
635 seasonal prediction for western North Pacific typhoons based on APCC multi-  
636 models. *Clim. Dyn.*, **48**, 71–88, <https://doi.org/10.1007/s00382-016-3063-1>.

637 King, D., J. Davidson, and L. Anderson-Berry, 2010: Disaster Mitigation and Societal  
638 Impacts. *Global Perspectives on Tropical Cyclones: From Science to Mitigation*,  
639 C. Johnny C L and K. Jeffrey D, Eds., World Scientific, 409–436.

640 Kossin, J. P., 2017: Hurricane intensification along United States coast suppressed  
641 during active hurricane periods. *Nature*, **541**, 390–393,  
642 <https://doi.org/10.1038/nature20783>.

643 Lander, M. A., 1994: An Exploratory Analysis of the Relationship between Tropical  
644 Storm Formation in the Western North Pacific and ENSO. *Mon. Weather Rev.*,  
645 **122**, 636–651, [https://doi.org/10.1175/1520-0493\(1994\)122<0636:AEAOTR>2.0.CO;2](https://doi.org/10.1175/1520-0493(1994)122<0636:AEAOTR>2.0.CO;2).

647 Lee, J.-Y., S.-S. Lee, B. Wang, K.-J. Ha, and J.-G. Jhun, 2013: Seasonal prediction  
648 and predictability of the Asian winter temperature variability. *Clim. Dyn.*, **41**,  
649 573–587, <https://doi.org/10.1007/s00382-012-1588-5>.

650 Liu, B., and C. Zhu, 2016: A possible precursor of the South China Sea summer  
651 monsoon onset: Effect of the South Asian High. *Geophys. Res. Lett.*, **43**, 11,072–

652 11,079, <https://doi.org/10.1002/2016GL071083>.

653 Lu, M.-M., P.-S. Chu, and Y.-C. Lin, 2010: Seasonal Prediction of Tropical Cyclone  
654 Activity Near Taiwan Using the Bayesian Multivariate Regression Method.  
655 *Weather Forecast.*, **25**, 1780–1795, <https://doi.org/10.1175/2010WAF2222408.1>.

656 Manganello, J. V, and Coauthors, 2016: Seasonal Forecasts of Tropical Cyclone  
657 Activity in a High-Atmospheric-Resolution Coupled Prediction System. *J. Clim.*,  
658 **29**, 1179–1200, <https://doi.org/10.1175/JCLI-D-15-0531.1>.

659 Michaelsen, J., 1987: Cross-Validation in Statistical Climate Forecast Models. *J.*  
660 *Clim. Appl. Meteorol.*, **26**, 1589–1600, [https://doi.org/10.1175/1520-](https://doi.org/10.1175/1520-0450(1987)026<1589:CVISCF>2.0.CO;2)  
661 [0450\(1987\)026<1589:CVISCF>2.0.CO;2](https://doi.org/10.1175/1520-0450(1987)026<1589:CVISCF>2.0.CO;2).

662 Murakami, H., and B. Wang, 2010: Future change of North Atlantic tropical cyclone  
663 tracks: Projection by a 20-km-mesh global atmospheric model. *J. Clim.*, **23**,  
664 2699–2721, <https://doi.org/10.1175/2010JCLI3338.1>.

665 Murphy, A. H., 1988: Skill Scores Based on the Mean Square Error and Their  
666 Relationships to the Correlation Coefficient. *Mon. Weather Rev.*, **116**, 2417–  
667 2424, [https://doi.org/10.1175/1520-0493\(1988\)116<2417:SSBOTM>2.0.CO;2](https://doi.org/10.1175/1520-0493(1988)116<2417:SSBOTM>2.0.CO;2).

668 Nicholls, N., 1979: A Possible Method for Predicting Seasonal Tropical Cyclone  
669 Activity in the Australian Region. *Mon. Weather Rev.*, **107**, 1221–1224,  
670 [https://doi.org/10.1175/1520-0493\(1979\)107<1221:APMFPS>2.0.CO;2](https://doi.org/10.1175/1520-0493(1979)107<1221:APMFPS>2.0.CO;2).

671 Peduzzi, P., B. Chatenoux, H. Dao, A. De Bono, C. Herold, J. Kossin, F. Mouton, and  
672 O. Nordbeck, 2012: Global trends in tropical cyclone risk. *Nat. Clim. Chang.*, **2**,  
673 289–294, <https://doi.org/10.1038/nclimate1410>.

674 Pielke, R. A., J. Gratz, C. W. Landsea, D. Collins, M. A. Saunders, and R. Musulin,

675        2008: Normalized Hurricane Damage in the United States: 1900–2005. *Nat.*  
 676        *Hazards Rev.*, **9**, 29–42, [https://doi.org/10.1061/\(ASCE\)1527-](https://doi.org/10.1061/(ASCE)1527-6988(2008)9:1(29))  
 677        6988(2008)9:1(29).

678        Tao, L., L. Wu, Y. Wang, and J. Yang, 2012: Influence of Tropical Indian Ocean  
 679        Warming and ENSO on Tropical Cyclone Activity over the Western North  
 680        Pacific. *J. Meteorol. Soc. Japan*, **90**, 127–144, [https://doi.org/10.2151/jmsj.2012-](https://doi.org/10.2151/jmsj.2012-107)  
 681        107.

682        Vecchi, G. A., and Coauthors, 2014: On the Seasonal Forecasting of Regional  
 683        Tropical Cyclone Activity. *J. Clim.*, **27**, 7994–8016,  
 684        <https://doi.org/10.1175/JCLI-D-14-00158.1>.

685        Wang, B., and J. C. L. Chan, 2002: How strong ENSO events affect tropical storm  
 686        activity over the western North Pacific. *J. Clim.*, **15**, 1643–1658,  
 687        [https://doi.org/10.1175/1520-0442\(2002\)015<1643:HSEEAT>2.0.CO;2](https://doi.org/10.1175/1520-0442(2002)015<1643:HSEEAT>2.0.CO;2).

688        ———, R. Wu, and X. Fu, 2000: Pacific–East Asian Teleconnection: How Does ENSO  
 689        Affect East Asian Climate? *J. Clim.*, **13**, 1517–1536,  
 690        [https://doi.org/10.1175/1520-0442\(2000\)013<1517:PEATHD>2.0.CO;2](https://doi.org/10.1175/1520-0442(2000)013<1517:PEATHD>2.0.CO;2).

691        ———, ———, and T. I. M. Li, 2003: Atmosphere–Warm Ocean Interaction and Its  
 692        Impacts on Asian–Australian Monsoon Variation\*. *J. Clim.*, **16**, 1195–1211,  
 693        [https://doi.org/10.1175/1520-0442\(2003\)16<1195:AOIAII>2.0.CO;2](https://doi.org/10.1175/1520-0442(2003)16<1195:AOIAII>2.0.CO;2).

694        Wang, B., Q. Ding, X. Fu, I.-S. Kang, K. Jin, J. Shukla, and F. Doblas-Reyes, 2005:  
 695        Fundamental challenge in simulation and prediction of summer monsoon  
 696        rainfall. *Geophys. Res. Lett.*, **32**, 15711, <https://doi.org/10.1029/2005GL022734>.

697        Wang, B., Y. Yang, Q.-H. Ding, H. Murakami, and F. Huang, 2010: Climate control

698 of the global tropical storm days (1965-2008). *Geophys. Res. Lett.*, **37**, n/a-n/a,  
699 <https://doi.org/10.1029/2010GL042487>.

700 ———, B. Xiang, and J.-Y. Lee, 2013: Subtropical High predictability establishes a  
701 promising way for monsoon and tropical storm predictions. *Proc. Natl. Acad.*  
702 *Sci.*, **110**, 2718–2722, <https://doi.org/10.1073/pnas.1214626110>.

703 ———, J.-Y. Lee, and B. Xiang, 2015a: Asian summer monsoon rainfall predictability:  
704 a predictable mode analysis. *Clim. Dyn.*, **44**, 61–74,  
705 <https://doi.org/10.1007/s00382-014-2218-1>.

706 ———, B. Xiang, J. Li, P. J. Webster, M. N. Rajeevan, J. Liu, and K.-J. Ha, 2015b:  
707 Rethinking Indian monsoon rainfall prediction in the context of recent global  
708 warming. *Nat. Commun.*, **6**, 7154, <https://doi.org/10.1038/ncomms8154>.

709 ———, J. Li, and Q. He, 2017: Variable and robust East Asian monsoon rainfall  
710 response to El Niño over the past 60 years (1957–2016). *Adv. Atmos. Sci.*, **34**,  
711 1235–1248, <https://doi.org/10.1007/s00376-017-7016-3>.

712 Wang, C., and L. Wu, 2012: Tropical Cyclone Intensity Change in the Western North  
713 Pacific: Downscaling from IPCC AR4 Experiments. *J. Meteorol. Soc. Japan*, **90**,  
714 223–233, <https://doi.org/10.2151/jmsj.2012-205>.

715 ———, and ———, 2016: Interannual Shift of the Tropical Upper-Tropospheric Trough  
716 and Its Influence on Tropical Cyclone Formation over the Western North Pacific.  
717 *J. Clim.*, **29**, 4203–4211, <https://doi.org/10.1175/JCLI-D-15-0653.1>.

718 ———, and ———, 2018a: Future Changes of the Monsoon Trough: Sensitivity to Sea  
719 Surface Temperature Gradient and Implications for Tropical Cyclone Activity.  
720 *Earth's Futur.*, **6**, 919–936, <https://doi.org/10.1029/2018EF000858>.

- 721 ———, and ———, 2018b: Projection of North Pacific Tropical Upper-Tropospheric  
 722 Trough in CMIP5 Models: Implications for Changes in Tropical Cyclone  
 723 Formation Locations. *J. Clim.*, **31**, 761–774, [https://doi.org/10.1175/JCLI-D-17-](https://doi.org/10.1175/JCLI-D-17-0292.1)  
 724 0292.1.
- 725 ———, and B. Wang, 2019: Tropical cyclone predictability shaped by western Pacific  
 726 subtropical high: integration of trans-basin sea surface temperature effects. *Clim.*  
 727 *Dyn.*, **0**, 0, <https://doi.org/10.1007/s00382-019-04651-1>.
- 728 ———, ———, and L. Wu, 2019a: Abrupt breakdown of the predictability of early season  
 729 typhoon frequency at the beginning of the twenty-first century. *Clim. Dyn.*, **52**,  
 730 3809–3822, <https://doi.org/10.1007/s00382-018-4350-9>.
- 731 ———, L. Wu, H. Zhao, J. Cao, and W. Tian, 2019b: Is there a quiescent typhoon  
 732 season over the western North Pacific following a strong El Niño event? *Int. J.*  
 733 *Climatol.*, **39**, 61–73, <https://doi.org/10.1002/joc.5782>.
- 734 Wang, G., J. Su, Y. Ding, and D. Chen, 2007a: Tropical cyclone genesis over the  
 735 south China sea. *J. Mar. Syst.*, **68**, 318–326,  
 736 <https://doi.org/10.1016/J.JMARSYS.2006.12.002>.
- 737 Wang, H., and K. Fan, 2007: Relationship between the Antarctic oscillation in the  
 738 western North Pacific typhoon frequency. *Chinese Sci. Bull.*, **52**, 561–565,  
 739 <https://doi.org/10.1007/s11434-007-0040-4>.
- 740 ———, J. Sun, and K. Fan, 2007b: Relationships between the North Pacific Oscillation  
 741 and the typhoon/hurricane frequencies. *Sci. China Ser. D Earth Sci.*, **50**, 1409–  
 742 1416, <https://doi.org/10.1007/s11430-007-0097-6>.
- 743 Wang, X., W. Zhou, C. Li, and D. Wang, 2012: Effects of the East Asian summer

monsoon on tropical cyclone genesis over the South China Sea on an  
interdecadal time scale. *Adv. Atmos. Sci.*, **29**, 249–262,  
<https://doi.org/10.1007/s00376-011-1080-x>.

Wilks, D. S., 2006: *Statistical Methods in the Atmospheric Sciences*. Academic Press,  
676 pp.

Wu, G., and Coauthors, 2007: The influence of mechanical and thermal forcing by the  
Tibetan Plateau on Asian climate. *J. Hydrometeorol.*, **8**, 770–789.

Wu, L., C. Wang, and B. Wang, 2015: Westward shift of western North Pacific  
tropical cyclogenesis. *Geophys. Res. Lett.*, **42**, 1537–1542,  
<https://doi.org/10.1002/2015GL063450>.

Xiang, B., B. Wang, W. Yu, and S. Xu, 2013: How can anomalous western North  
Pacific Subtropical High intensify in late summer? *Geophys. Res. Lett.*, **40**,  
2349–2354, <https://doi.org/10.1002/grl.50431>.

Xie, S.-P., K. Hu, J. Hafner, H. Tokinaga, Y. Du, G. Huang, and T. Sampe, 2009:  
Indian Ocean Capacitor Effect on Indo–Western Pacific Climate during the  
Summer following El Niño. *J. Clim.*, **22**, 730–747,  
<https://doi.org/10.1175/2008JCLI2544.1>.

———, Y. Kosaka, Y. Du, K. Hu, J. S. Chowdary, and G. Huang, 2016: Indo-western  
Pacific ocean capacitor and coherent climate anomalies in post-ENSO summer:  
A review. *Adv. Atmos. Sci.*, **33**, 411–432, <https://doi.org/10.1007/s00376-015-5192-6>.

Xie, S., and S. G. H. Phlander, 1994: A coupled ocean-atmosphere model of relevance  
to the ITCZ in the eastern Pacific. *Tellus A*, **46**, 340–350,



767 <https://doi.org/10.1034/j.1600-0870.1994.t01-1-00001.x>.

768 Xuan, S., Q. Zhang, and S. Sun, 2011: Anomalous midsummer rainfall in Yangtze  
 769 River-Huaihe River valleys and its association with the East Asia westerly jet.  
 770 *Adv. Atmos. Sci.*, **28**, 387–397, <https://doi.org/10.1007/s00376-010-0111-3>.

771 Yan, Z. Bin, Z. H. Lin, and H. Zhang, 2015: The Relationship between the East Asian  
 772 Subtropical Westerly Jet and Summer Precipitation over East Asia as Simulated  
 773 by the IAP AGCM4 . 0 The Relationship between the East Asian Subtropical  
 774 Westerly Jet and Summer Precipitation over East Asia as Simulate. *Atmos.*  
 775 *Ocean. Sci. Lett.*, **7**, 487–492, <https://doi.org/10.3878/AOSL20140048>.

776 Yim, S.-Y., B. Wang, and W. Xing, 2014: Prediction of early summer rainfall over  
 777 South China by a physical-empirical model. *Clim. Dyn.*, **43**, 1883–1891,  
 778 <https://doi.org/10.1007/s00382-013-2014-3>.

779 Zhan, R., and Y. Wang, 2016: CFSv2-based statistical prediction for seasonal  
 780 accumulated cyclone energy (ACE) over the western North Pacific. *J. Clim.*, **29**,  
 781 525–541, <https://doi.org/10.1175/JCLI-D-15-0059.1>.

782 ———, ———, and X. Lei, 2011a: Contributions of ENSO and East Indian Ocean SSTA  
 783 to the interannual variability of Northwest Pacific Tropical cyclone frequency. *J.*  
 784 *Clim.*, **24**, 509–521, <https://doi.org/10.1175/2010JCLI3808.1>.

785 ———, ———, and C. C. Wu, 2011b: Impact of SSTA in the East Indian Ocean on the  
 786 frequency of Northwest Pacific tropical cyclones: A regional atmospheric model  
 787 study. *J. Clim.*, **24**, 6227–6242, <https://doi.org/10.1175/JCLI-D-10-05014.1>.

788 ———, ———, and M. Ying, 2012: Seasonal forecasts of tropical cyclone activity over  
 789 the western North Pacific: A review. *Trop. Cyclone Res. Rev.*, **1**, 307–324,

790 <https://doi.org/10.6057/2012TCRR03.07>.

791 ———, ———, and M. Wen, 2013: The SST Gradient between the Southwestern Pacific  
792 and the Western Pacific Warm Pool: A New Factor Controlling the Northwestern  
793 Pacific Tropical Cyclone Genesis Frequency. *J. Clim.*, **26**, 2408–2415,  
794 <https://doi.org/10.1175/jcli-d-12-00798.1>.

795 Zhang, Q., L. Wu, and Q. Liu, 2009: Tropical Cyclone Damages in China 1983–2006.  
796 *Bull. Am. Meteorol. Soc.*, **90**, 489–496,  
797 <https://doi.org/10.1175/2008BAMS2631.1>.

798 Zhang, W., G. A. Vecchi, H. Murakami, G. Villarini, and L. Jia, 2016a: The Pacific  
799 Meridional Mode and the Occurrence of Tropical Cyclones in the Western North  
800 Pacific. *J. Clim.*, **29**, 381–398, <https://doi.org/10.1175/JCLI-D-15-0282.1>.

801 Zhang, W., G. Villarini, G. A. Vecchi, H. Murakami, and R. Gudgel, 2016b:  
802 Statistical-dynamical seasonal forecast of western North Pacific and East Asia  
803 landfalling tropical cyclones using the high-resolution GFDL FLOR coupled  
804 model. *J. Adv. Model. Earth Syst.*, **8**, 538–565,  
805 <https://doi.org/10.1002/2015MS000607>.

806 Zhang, X., S. Zhong, Z. Wu, and Y. Li, 2018: Seasonal prediction of the typhoon  
807 genesis frequency over the Western North Pacific with a Poisson regression  
808 model. *Clim. Dyn.*, **51**, 4585–4600, <https://doi.org/10.1007/s00382-017-3654-5>.

809 Zhao, H., 2016: A downscaling technique to simulate changes in western North  
810 Pacific tropical cyclone activity between two types of El Niño events. *Theor.*  
811 *Appl. Climatol.*, **123**, 487–501, <https://doi.org/10.1007/s00704-015-1374-5>.

812 ———, and C. Wang, 2016: Interdecadal modulation on the relationship between

813 ENSO and typhoon activity during the late season in the western North Pacific.

814 *Clim. Dyn.*, **47**, 315–328, <https://doi.org/10.1007/s00382-015-2837-1>.

815 ———, and ———, 2019: On the relationship between ENSO and tropical cyclones in the

816 western North Pacific during the boreal summer. *Clim. Dyn.*, **52**, 275–288,

817 <https://doi.org/10.1007/s00382-018-4136-0>.

818 ———, L. Wu, and W. Zhou, 2010: Assessing the influence of the ENSO on tropical

819 cyclone prevailing tracks in the western North Pacific. *Adv. Atmos. Sci.*, **27**,

820 1361–1371, <https://doi.org/10.1007/s00376-010-9161-9>.

821 Zhou, B., and X. Cui, 2008: Hadley circulation signal in the tropical cyclone

822 frequency over the western North Pacific. *J. Geophys. Res.*, **113**,

823 <https://doi.org/10.1029/2007jd009156>.

824 Zhou, B., and X. Cui, 2010: Sea surface temperature east of Australia: A predictor of

825 tropical cyclone frequency over the western North Pacific? *Chinese Sci. Bull.*,

826 **56**, 196–201, <https://doi.org/10.1007/s11434-010-4157-5>.

827  
828  
829 **Table captions:**

830 Table 1 Definitions of predictors for TCG in individual sub-regions

831 Table 2 Correlation ecoefficiency between the observed TC genesis frequency and

832 cross-validated reforecast (1965-1999) and prediction (2000-2016) during July-

833 October in individual subregions and the WNP. The significant correlations are bold.

834 **Tables:**

Table 1 Definitions of predictors for TCG in individual sub-regions

Name	Definition	Meaning
NW-I	May-June mean SST over (5°S–10°N, 180°–130°W)	Central Pacific SST predictor
NW-II	May-June minus October–November SST tendency over (5°S–20°N, 50°E–100°E)	Indian Ocean SST predictor
SE-I	May-June mean SST over (10°S–10°N, 180°–130°W)	Central Pacific SST predictor
SE-II	May-June minus October–November SST tendency over (10°S–10°N, 180°–220°E)	Central Pacific SST tendency predictor
NE-I	May-June mean SST (10°S–10°N, 130°W–80°W) minus SST (10°N–25°N, 160°E–160°W)	Pacific dipole SST predictor
NE-II	May-June minus September–October 2m air temperature tendency over (0–30°N, 40°E–70°E)	West Indian Ocean T2m tendency predictor
SW-I	May-June minus November–December SLP tendency over (10°N–20°N, 140°E–180°)	WNP SLP tendency predictor
SW-II	May-June mean SST over (5°S–5°N, 170°W–100°W)	Central Pacific SST predictor
SCS-I	June 850 hPa zonal wind over (0°–10°N, 110°E–125°E) and (2.5°S–7.5°N, 125°E–140°E)	Indonesia zonal wind predictor
SCS-II	May-June minus March–April SST tendency over (5°N–20°N, 150°E–180°)	Eastern WNP SST tendency predictor

Table 2 Correlation coefficient between the observed TC genesis frequency and cross-validated reforecast (1965-1999) and prediction (2000-2016) during July–October in individual subregions and the WNP. The significant correlations are bold.

	SCS	SW	NW	SE	NE	WNP
1965-1999	<b>0.51</b>	0.1	<b>0.61</b>	<b>0.77</b>	<b>0.58</b>	<b>0.47</b>
2000-2016	<b>0.59</b>	0.38	<b>0.52</b>	<b>0.69</b>	<b>0.49</b>	<b>0.68</b>

**Figure captions:**

Figure 1 Climatological TC geneses and tracks over the WNP. TC genesis locations (green dots) and tracks (light blue lines) during July-September over 1965-2016. The grey dash lines indicate the boundaries of five sub-regions (i.e. South China Sea (SCS), southwest WNP (SW), northwest WNP (NW), southeast WNP(SE) and northeast WNP(NE)). Numbers represent the annual mean TC genesis frequency in individual sub-regions.

Figure 2 Large-scale circulation pattern and boundary condition anomalies favoring TCG in the northwest WNP. Simultaneous correlation map between TCG frequency in the northwest WNP and (a) SST (over ocean) and T2m (over land) (shadings) and 850 hPa wind (vectors) and (b) 500 hPa omega (shadings) and 200 hPa wind (vectors) in July-September during 1965–2000. The green vectors and dotted areas denote regions with correlation coefficients significant at 95% confidence level. The green boxes indicate boundaries of the northwest WNP.

Figure 3 The same as Figure 2 but for southeast WNP.

Figure 4 The same as Figure 2 but for northeast WNP.

Figure 5 Large-scale circulation pattern and boundary condition anomalies favoring TCG in the southwest WNP. Simultaneous correlation map between TCG frequency in the southwest WNP and (a) SST (over ocean) and T2m (over land) (shadings), SLP (contours) and 850 hPa wind (vectors) and (b) 500 hPa omega (shadings) and 200 hPa wind (vectors) in July-September during 1965–2000. The green vectors and dotted areas denote regions with correlation coefficients significant at 95% confidence level. The green boxes indicate boundaries of the southwest WNP.

Figure 6 Large-scale circulation patterns and boundary conditions anomalies favoring

TCG in the South China Sea. Simultaneous correlation map between TCG frequency in the South China Sea and (a) 200 hPa zonal wind (black contours) and 500 hPa omega (shadings), (b) 850 hPa winds (vectors) and vorticity (shadings) and (c) SST in July-September during 1965–2000. The green vectors in (b) and dotted areas denote regions with correlation coefficients significant at 95% confidence level. The vectors in (a) display the climatological 200 hPa wind, indicating the mean circulation associated with the South Asian high. The grey line in (a) shows the zero contour of climatological 200 hPa zonal wind, which denotes the ridge of the South Asian high. The green boxes indicate the boundaries of the South China Sea.

Figure 7 Predictors for TCG frequency in the northwest WNP. Correlation map between TCG frequency in the northwest WNP and (a) May-June mean SST and (b) SST tendency from September-October to May-June during 1965-2000. Dotted areas denote regions with correlation coefficients significant at 95% confidence level. The black boxes represent the locations of predictors and green boxes indicate boundaries of the northwest WNP.

Figure 8 The lead-lag correlation between predictors for TCG in the northwest WNP and July-September mean large-scale conditions. Correlation maps between NW-I and July-September mean (a) SST (b) SLP (shadings) and 850 hPa wind (vectors) and (c) 500 hPa omega during 1979–2000. (d)-(f) are the same as (a)-(c), but for predictor NW-II. The green vectors and dotted areas denote regions with correlation coefficients significant at 95% confidence level. The green boxes indicate boundaries of the northwest WNP.

Figure 9 Predictor for TCG frequency in the southeast WNP. Correlation map between TCG frequency over the southeast WNP and (a) May-June mean SST (b) SST tendency

from September-October to May-June during 1965-2000. Dotted areas denote regions with correlation coefficients significant at 95% confidence level. The black boxes represent the location of predictors and green boxes indicate boundaries of the southeast WNP.

Figure 10 The lead-lag correlation between predictors for TCG in the southeast WNP and July-September mean large-scale conditions. The correlation maps between predictor SE-I and July–September mean (a) SLP (shadings) and 850 hPa wind (vectors), (b) SST and (c) 500 hPa omega during 1965–2000. (d)-(f) are the same as (a)-(c), but for predictor SE-II.

Figure 11 Predictors for TCG frequency in the northeast WNP. Correlation map between TCG frequency over the northwest WNP and (a) May-June mean SST (b) 2m air temperature tendency from September-October to May-June during 1965-2000. Dotted areas denote regions with correlation coefficients significant at 95% confidence level. The black boxes represent the location of predictors and red boxes indicate boundaries of the northeast WNP.

Figure 12 The lead-lag correlation between predictors for TCG in the northeast WNP and July-September mean large-scale conditions. The correlation maps between predictor NE-I and July–September mean (a) SST (b) SLP (shadings) and 850 hPa wind (vectors), and (c) 500 hPa omega during 1965–2000. (d)-(f) are the same as (a)-(c), but for predictor NE-II. The green vectors and dotted areas denote regions with correlation coefficients significant at 95% confidence level. The green boxes indicate boundaries of the northeast WNP.

Figure 13 Predictors for TCG frequency in the southwest WNP. Correlation map between TC genesis frequency in the southwest WNP and (a) SLP tendency from

November-December to May-June (shading), and (b) May-June mean SST during 1965-2000. Dotted areas denote regions with correlation coefficients significant at 95% confidence level. The black boxes represent the location of predictors and green boxes indicate boundaries of the southwest WNP.

Figure 14 The lead-lag correlation between predictors for TCG in the southwest WNP and July-September mean large-scale conditions. The correlation maps between predictor SW-I and July-September mean (a) SLP (shadings), (b) SST (shadings) and 850 hPa wind (vectors), and (c) 500 hPa omega during 1965-2000. The correlation maps between predictor SW-II and July-September mean (a) SST (shadings), (b) SLP (shadings) and 850 hPa wind (vectors), and (c) 500 hPa omega during 1965-2000.

Figure 15 Predictors for TCG frequency in the South China Sea. Correlation map between TC genesis frequency in the South China Sea and (a) SLP tendency from November-December to May-June (shading), and (b) SST tendency from September-October to May-June during 1965-2000. Dotted areas denote regions with correlation coefficients significant at 95% confidence level. The black boxes represent the location of predictors and green boxes indicate boundaries of the South China Sea.

Figure 16 The lead-lag correlation between predictors for TCG in the South China Sea and July-September mean large-scale conditions. The correlation maps between predictor SCS-I and July-September mean (a) 850 hPa zonal wind (shadings), (b) 200 hPa zonal wind (shadings) and 200 hPa wind (vectors), and (c) 500 hPa omega during 1965-2000. The correlation maps between predictor SCS-II and July-September mean (d) SST (shadings), (e) SLP (shading) and 850 hPa (vectors), and (f) 500 hPa omega during 1965-2000. The grey line (b) shows the zero contour of climatological 200hPa zonal wind, which denotes the ridge of the South Asian high.



Figure 17 Predictability and prediction skill for the TCG frequency in individual sub-regions and the whole WNP. Time series of TC counts over the (a) northwest WNP (b) southeast WNP, (c) northeast WNP, (d) southwest WNP, (e) South China Sea and (f) WNP obtained from the JTWC best track (black line), cross-validated reforecast (blue line) and prediction (green line) from 1965-2016. The grey dash lines sperate the training and prediction period. The corresponding TCC is shown in each panel.

Figure 18 Correlation coefficient of predicted and observed seasonal TC genesis frequency in the SCS (blue squares), (b) southwest WNP (red squares), (c) northwest WNP (black squares), (d) southeast WNP (green squares), (e) northeast WNP (brown squares), and (f) WNP (purple squares) during 1965-2016. The black line denotes the 95% significant level.

# **Figures:**

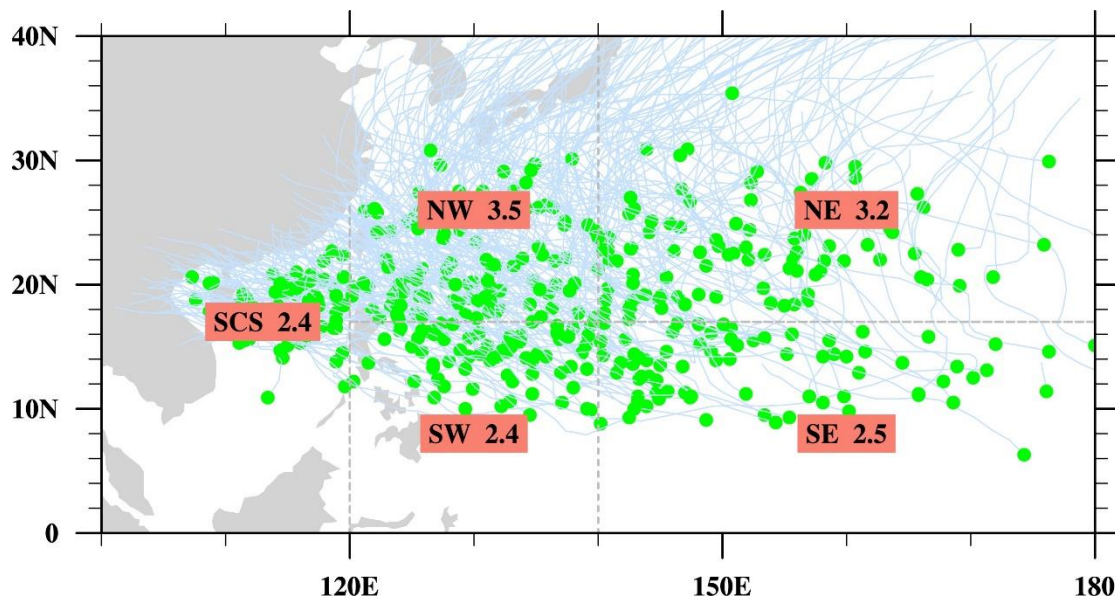


Figure 1 Climatological TC geneses and tracks over the WNP. TC genesis locations (green dots) and tracks (light blue lines) during July-September over 1965-2016. The grey dash lines indicate the boundaries of five sub-regions (i.e. South China Sea (SCS), southwest WNP (SW), northwest WNP (NW), southeast WNP(SE) and northeast WNP(NE)). Numbers represent the annual mean TC genesis frequency in individual sub-regions.

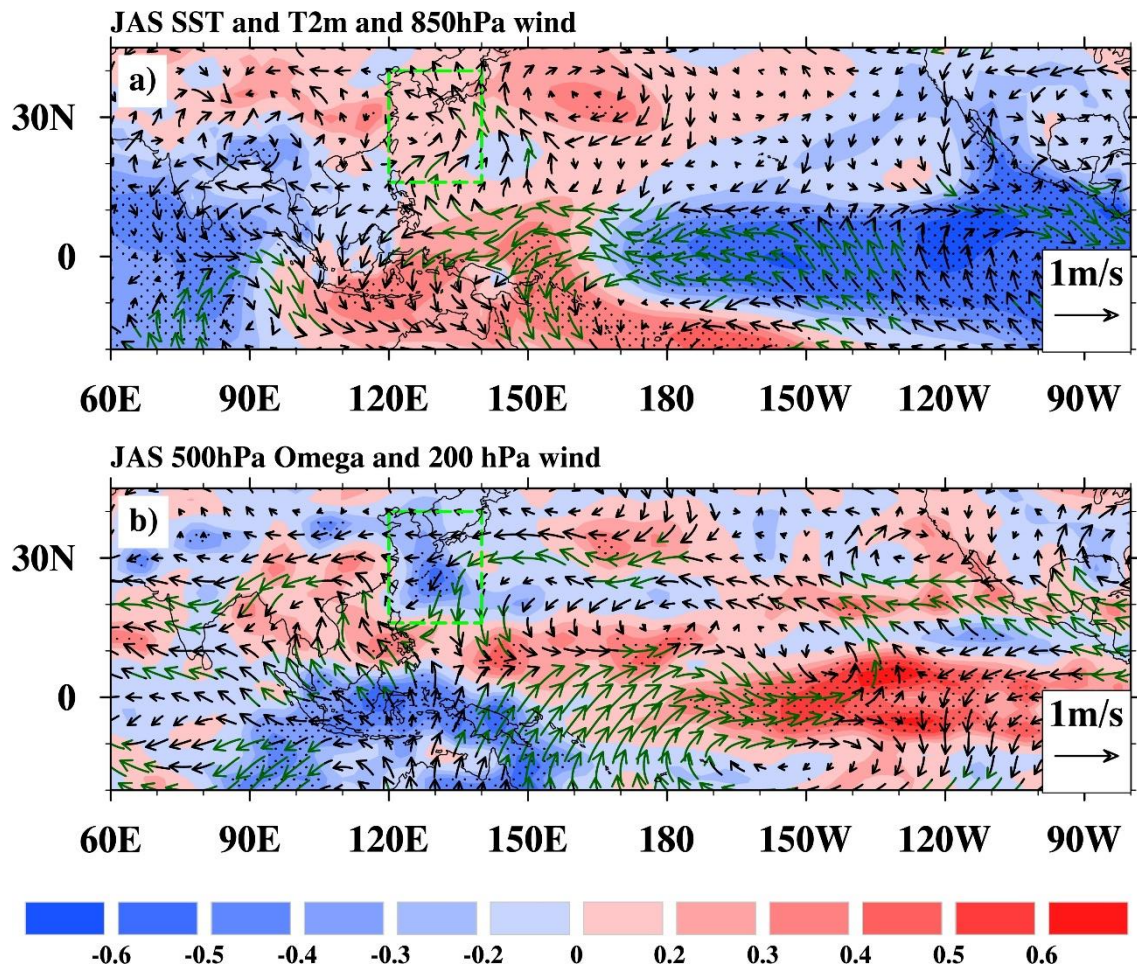


Figure 2 Large-scale circulation pattern and boundary condition anomalies favoring TCG in the northwest WNP. Simultaneous correlation map between TCG frequency in the northwest WNP and (a) SST (over ocean) and T2m (over land) (shadings) and 850 hPa wind (vectors) and (b) 500 hPa omega (shadings) and 200 hPa wind (vectors) in July-September during 1965–2000. The green vectors and dotted areas denote regions with correlation coefficients significant at 95% confidence level. The green boxes indicate boundaries of the northwest WNP.

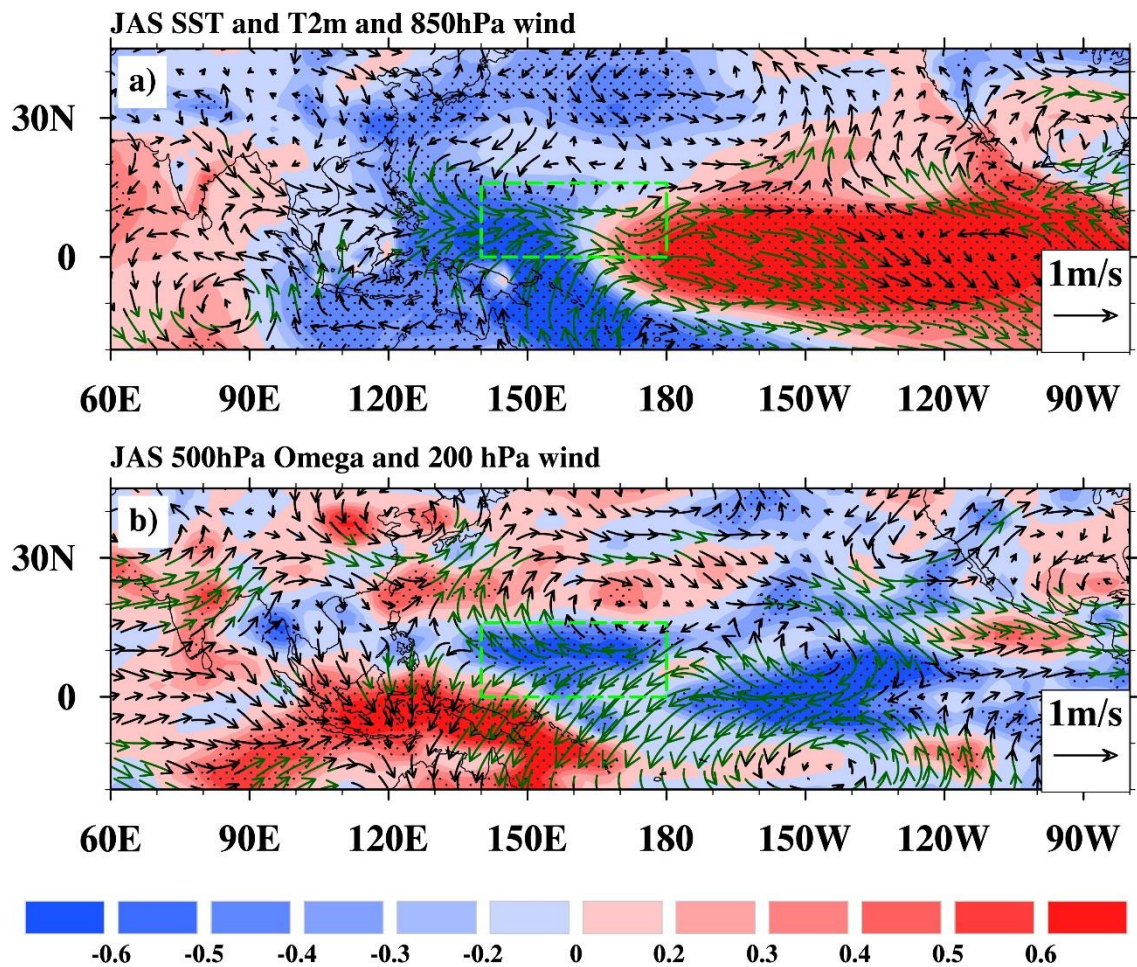


Figure 3 The same as Figure 2 but for southeast WNP.



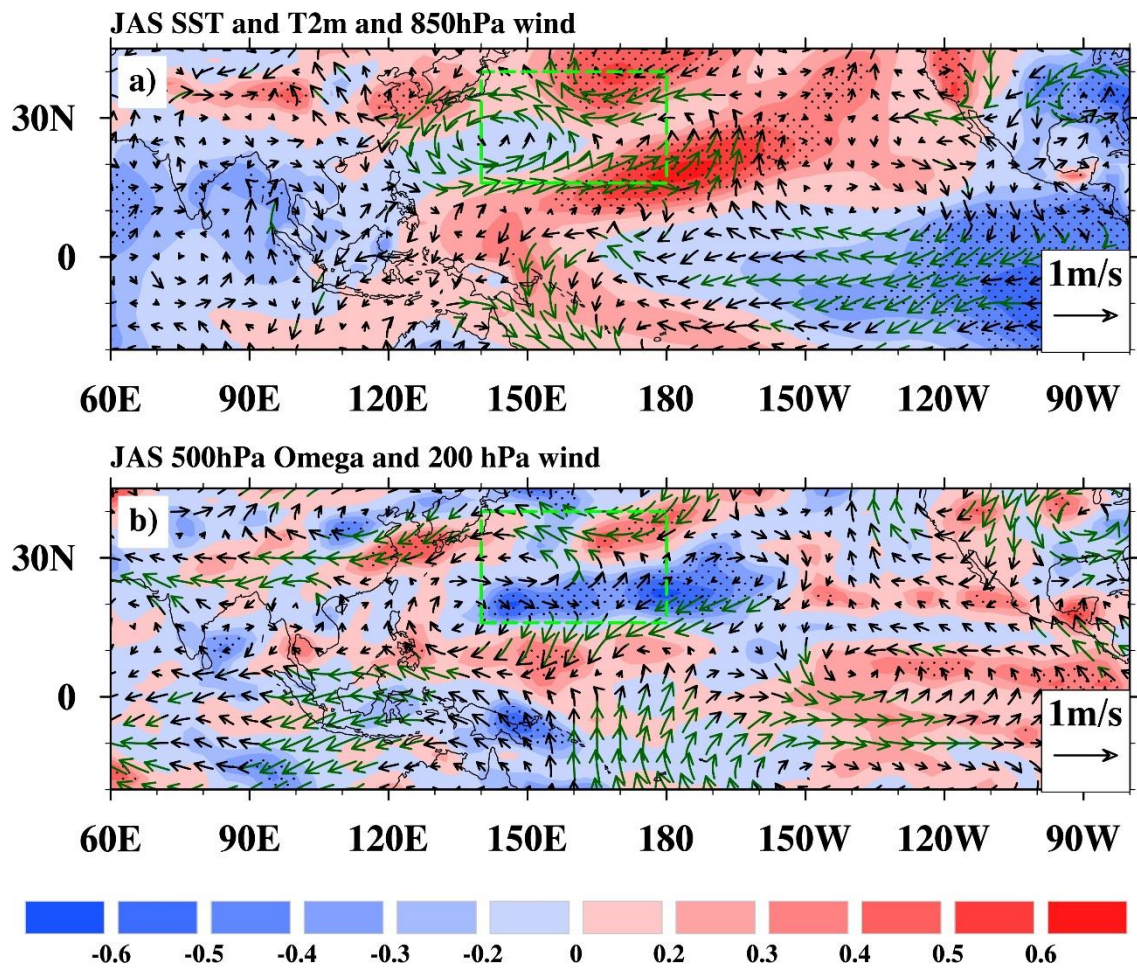


Figure 4 The same as Figure 2 but for northeast WNP.

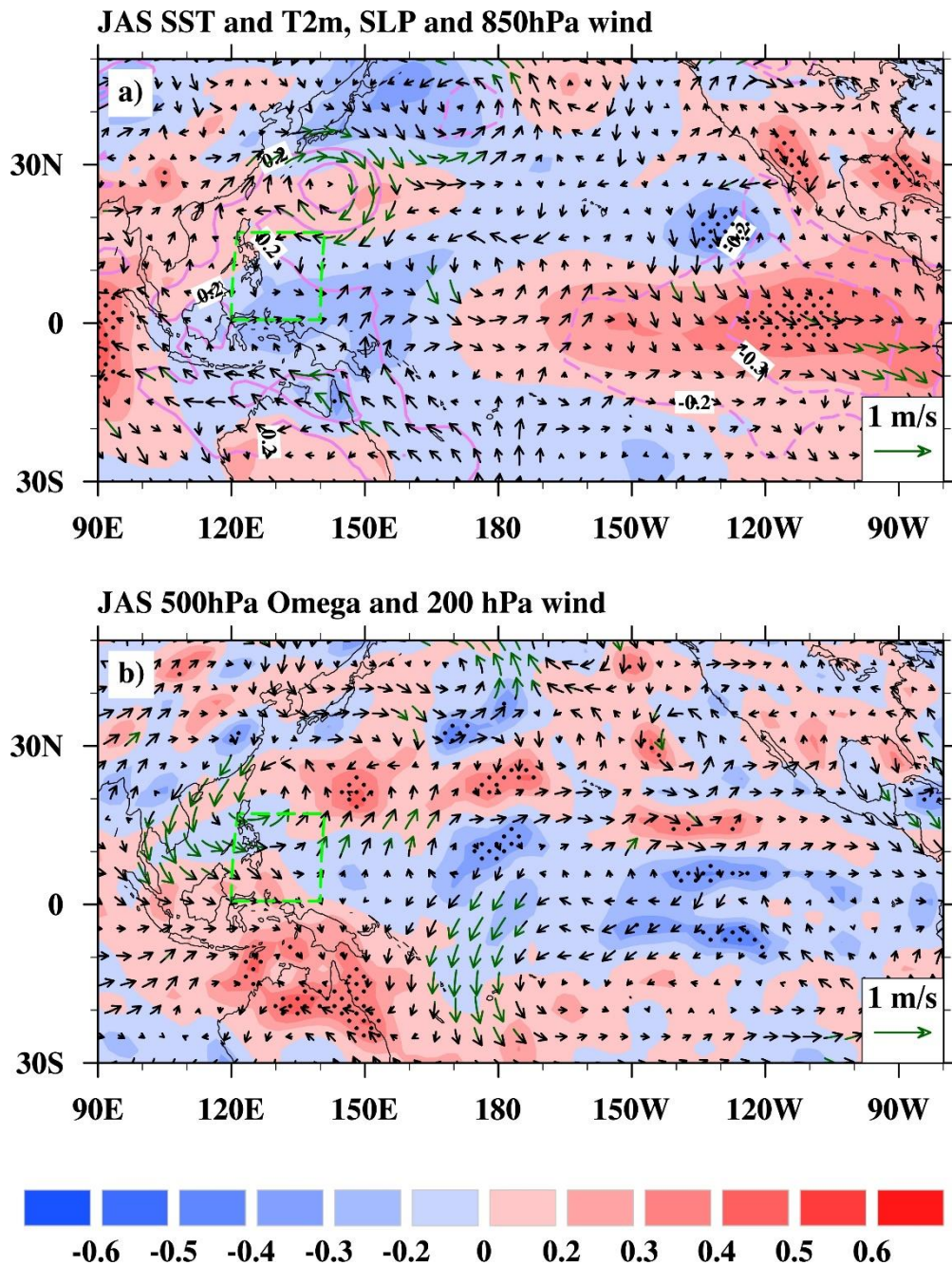


Figure 5 Large-scale circulation pattern and boundary condition anomalies favoring TCG in the southwest WNP. Simultaneous correlation map between TCG frequency in the southwest WNP and (a) SST (over ocean) and T2m (over land) (shadings), SLP (contours) and 850 hPa wind (vectors) and (b) 500 hPa omega (shadings) and 200 hPa wind (vectors) in July-September during 1965–2000. The green vectors and dotted areas denote regions with correlation coefficients significant at 95% confidence level. The green boxes indicate boundaries of the southwest WNP.



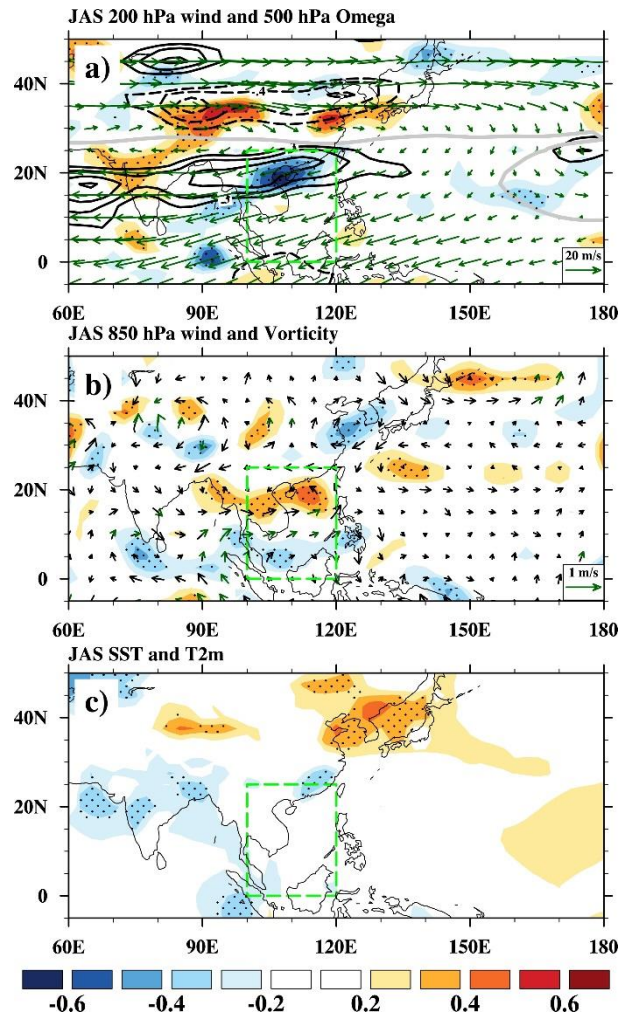


Figure 6 Large-scale circulation patterns and boundary conditions anomalies favoring TCG in the South China Sea. Simultaneous correlation map between TCG frequency in the South China Sea and (a) 200 hPa zonal wind (black contours) and 500 hPa omega(shadings), (b) 850 hPa winds (vectors) and vorticity (shadings) and (c) SST in July-September during 1965–2000. The green vectors in (b) and dotted areas denote regions with correlation coefficients significant at 95% confidence level. The vectors in (a) display the climatological 200 hPa wind, indicating the mean circulation associated with the South Asian high. The grey line in (a) shows the zero contour of climatological 200 hPa zonal wind, which denotes the ridge of the South Asian high. The green boxes indicate the boundaries of the South China Sea.

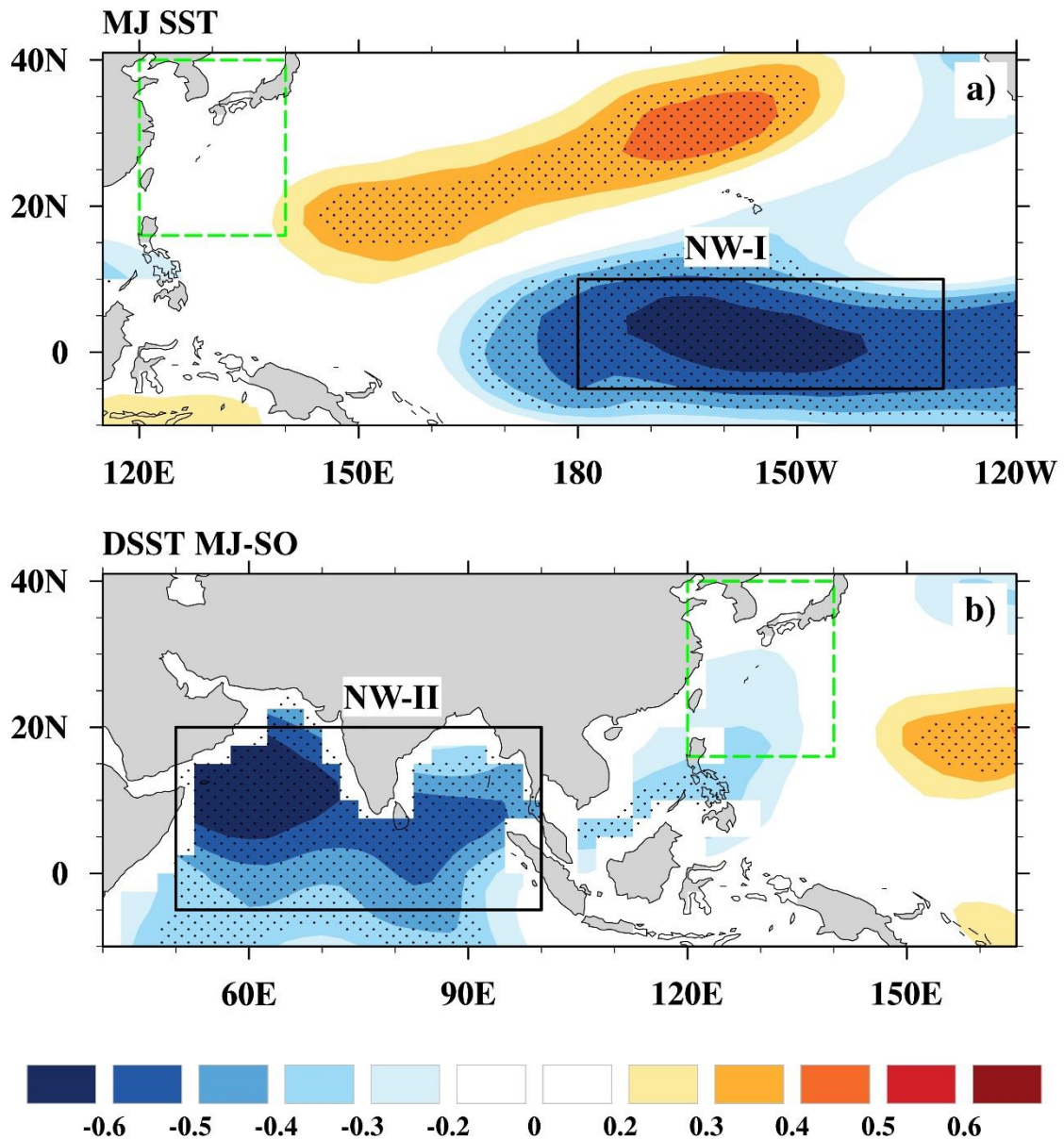


Figure 7 Predictors for TCG frequency in the northwest WNP. Correlation map between TCG frequency in the northwest WNP and (a) May-June mean SST and (b) SST tendency from September-October to May-June during 1965-2000. Dotted areas denote regions with correlation coefficients significant at 95% confidence level. The black boxes represent the locations of predictors and green boxes indicate boundaries of the northwest WNP.



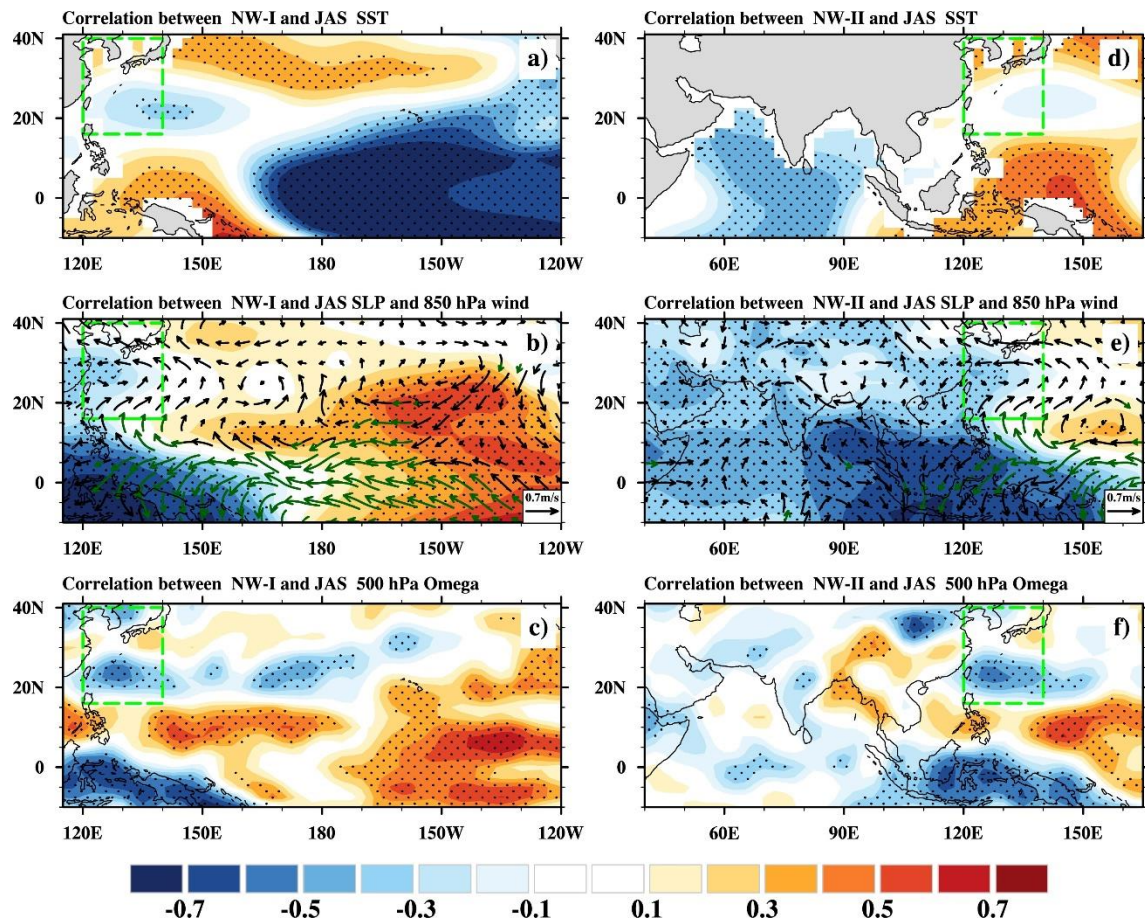


Figure 8 The lead-lag correlation between predictors for TCG in the northwest WNP and July-September mean large-scale conditions. Correlation maps between NW-I and July-September mean (a) SST (b) SLP (shadings) and 850 hPa wind (vectors) and (c) 500 hPa omega during 1979–2000. (d)-(f) are the same as (a)-(c), but for predictor NW-II. The green vectors and dotted areas denote regions with correlation coefficients significant at 95% confidence level. The green boxes indicate boundaries of the northwest WNP.

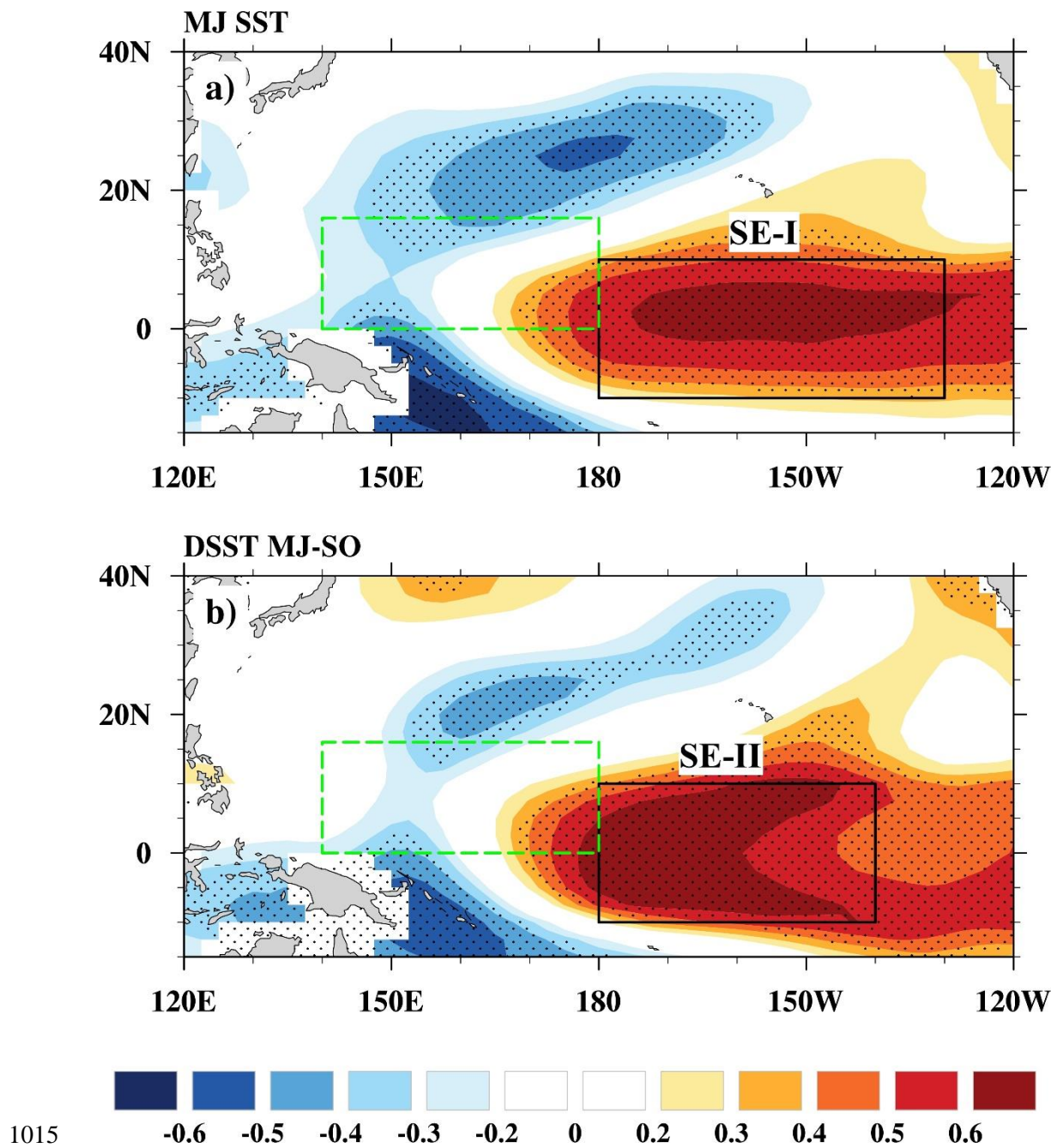
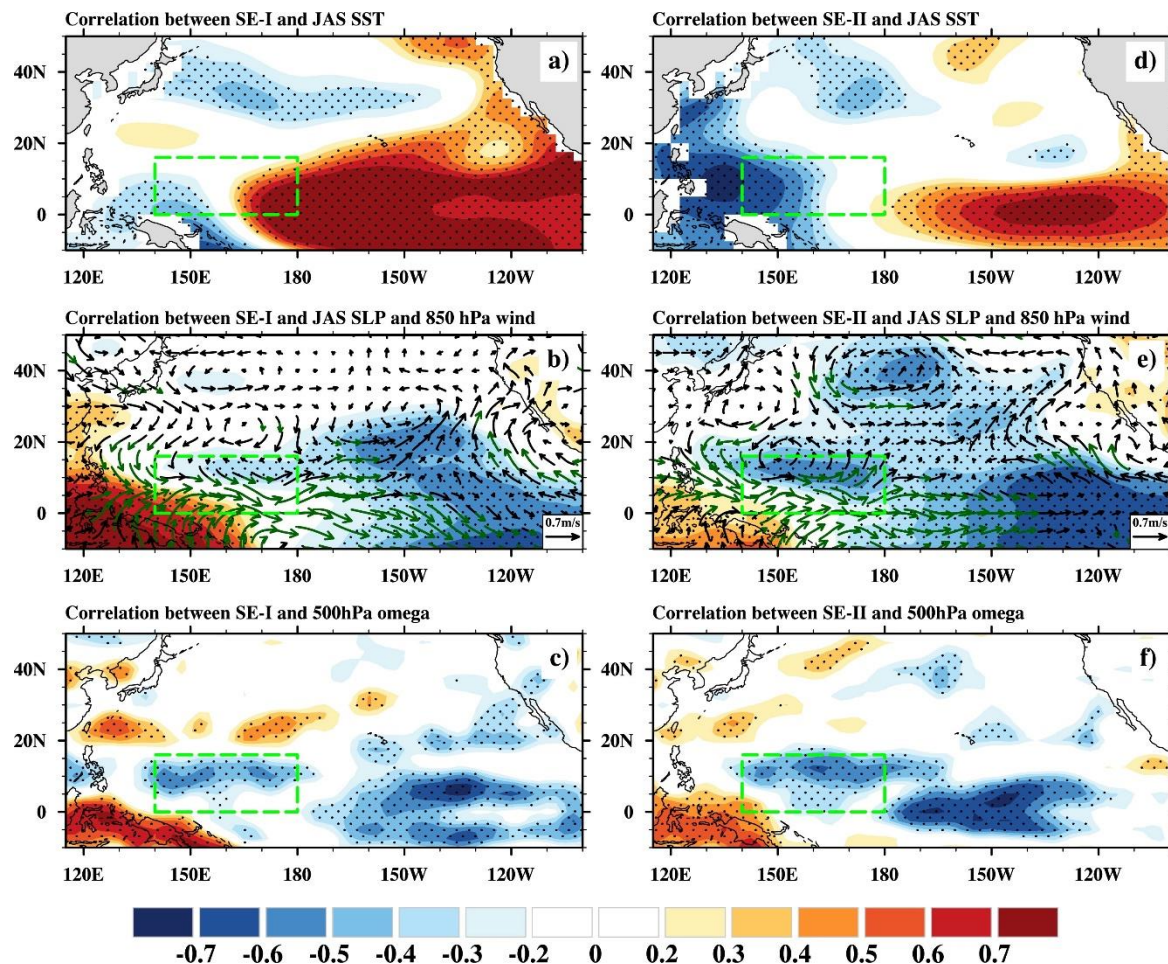


Figure 9 Predictor for TCG frequency in the southeast WNP. Correlation map between TCG frequency over the southeast WNP and (a) May-June mean SST (b) SST tendency from September-October to May-June during 1965-2000. Dotted areas denote regions with correlation coefficients significant at 95% confidence level. The black boxes represent the location of predictors and green boxes indicate boundaries of the southeast WNP.





1023

1024 Figure 10 The lead-lag correlation between predictors for TCG in the southeast WNP  
 1025 and July–September mean large-scale conditions. The correlation maps between  
 1026 predictor SE-I and July–September mean (a) SLP (shadings) and 850 hPa wind  
 1027 (vectors), (b) SST and (c) 500 hPa omega during 1965–2000. (d)–(f) are the same as  
 1028 (a)–(c), but for predictor SE-II. The green vectors and dotted areas denote regions with  
 1029 correlation coefficients significant at 95% confidence level. The green boxes indicate  
 1030 boundaries of the southeast WNP.

1031

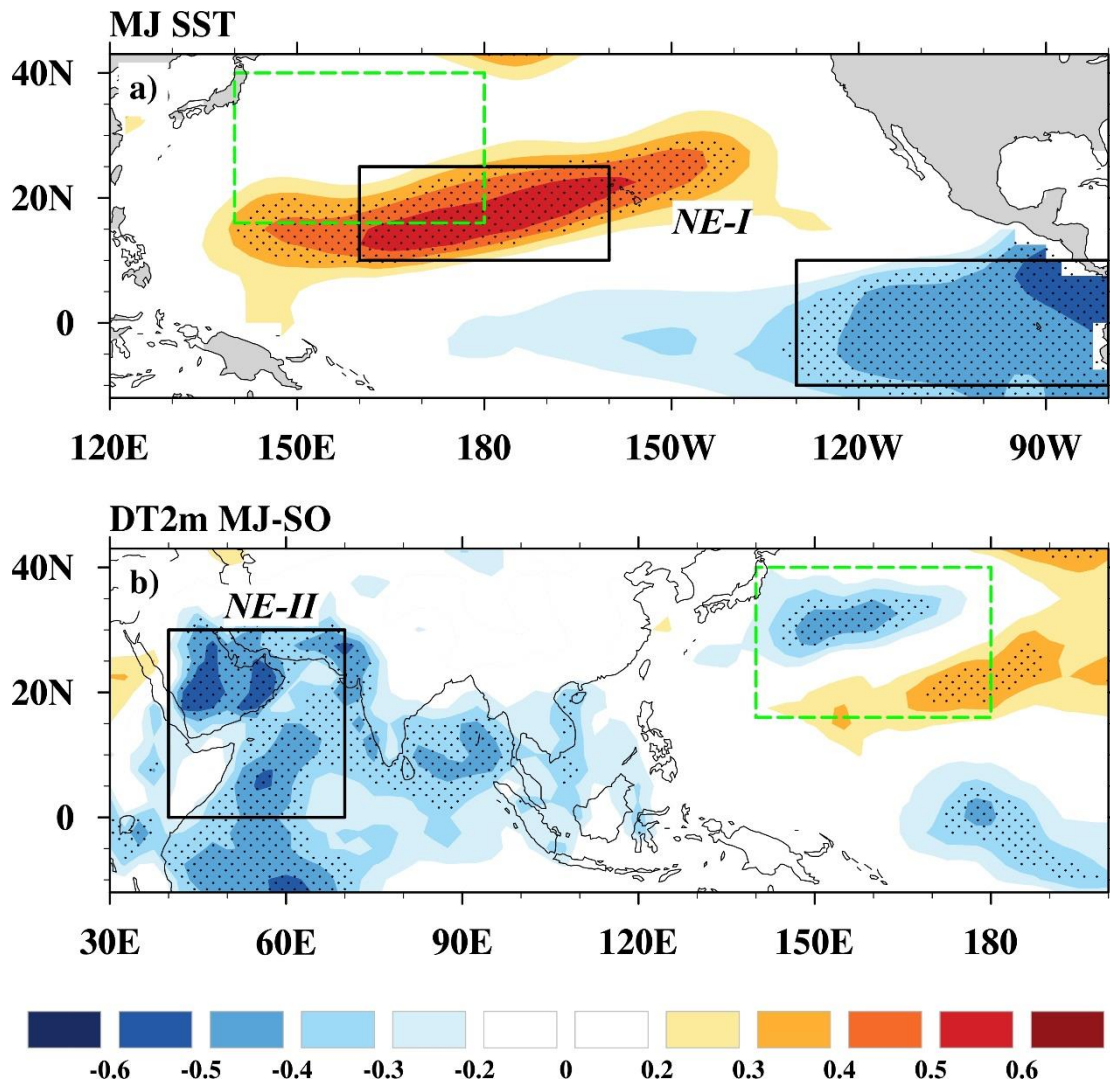


Figure 11 Predictors for TCG frequency in the northeast WNP. Correlation map between TCG frequency over the northwest WNP and (a) May-June mean SST (b) 2m air temperature tendency from September-October to May-June during 1965-2000. Dotted areas denote regions with correlation coefficients significant at 95% confidence level. The black boxes represent the location of predictors and red boxes indicate boundaries of the northeast WNP.

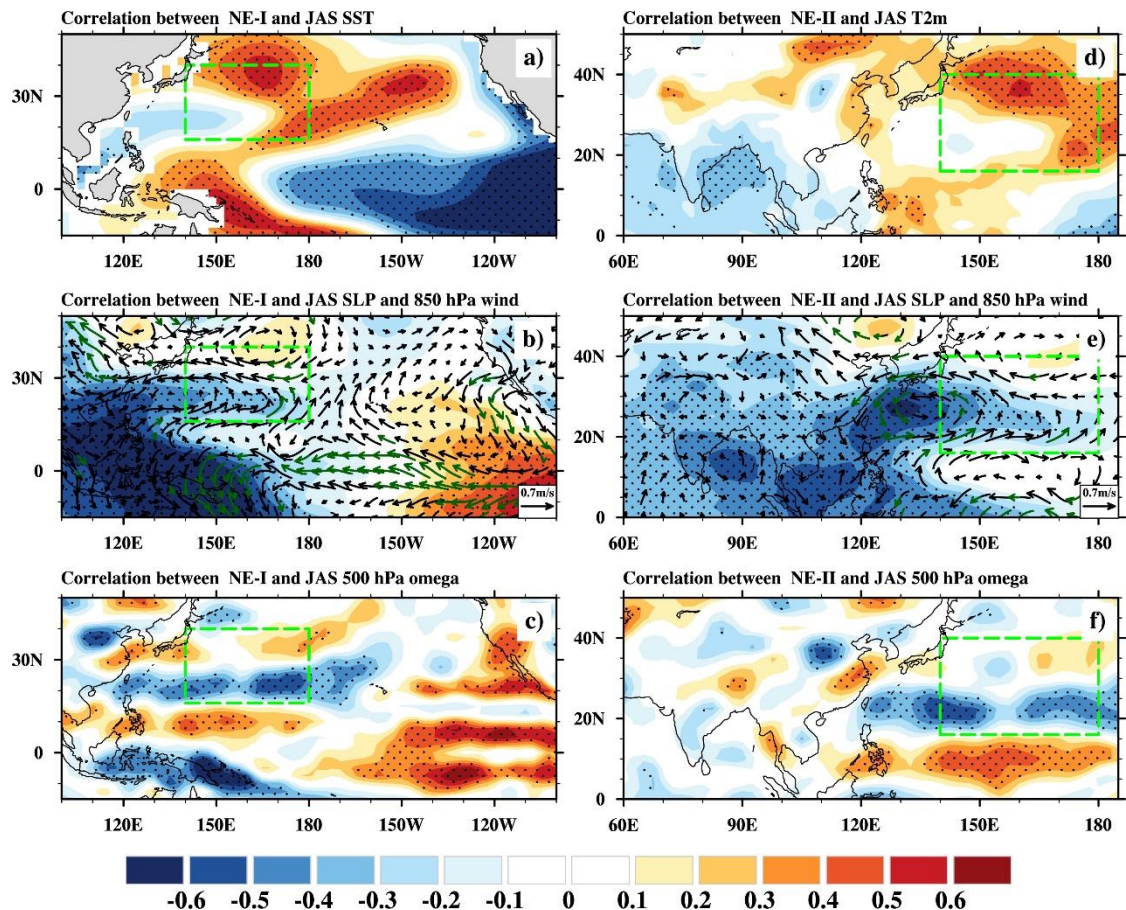


Figure 12 The lead-lag correlation between predictors for TCG in the northeast WNP and July–September mean large-scale conditions. The correlation maps between predictor NE-I and July–September mean (a) SST (b) SLP (shadings) and 850 hPa wind (vectors), and (c) 500 hPa omega during 1965–2000. (d)–(f) are the same as (a)–(c), but for predictor NE-II. The green vectors and dotted areas denote regions with correlation coefficients significant at 95% confidence level. The green boxes indicate boundaries of the northeast WNP.



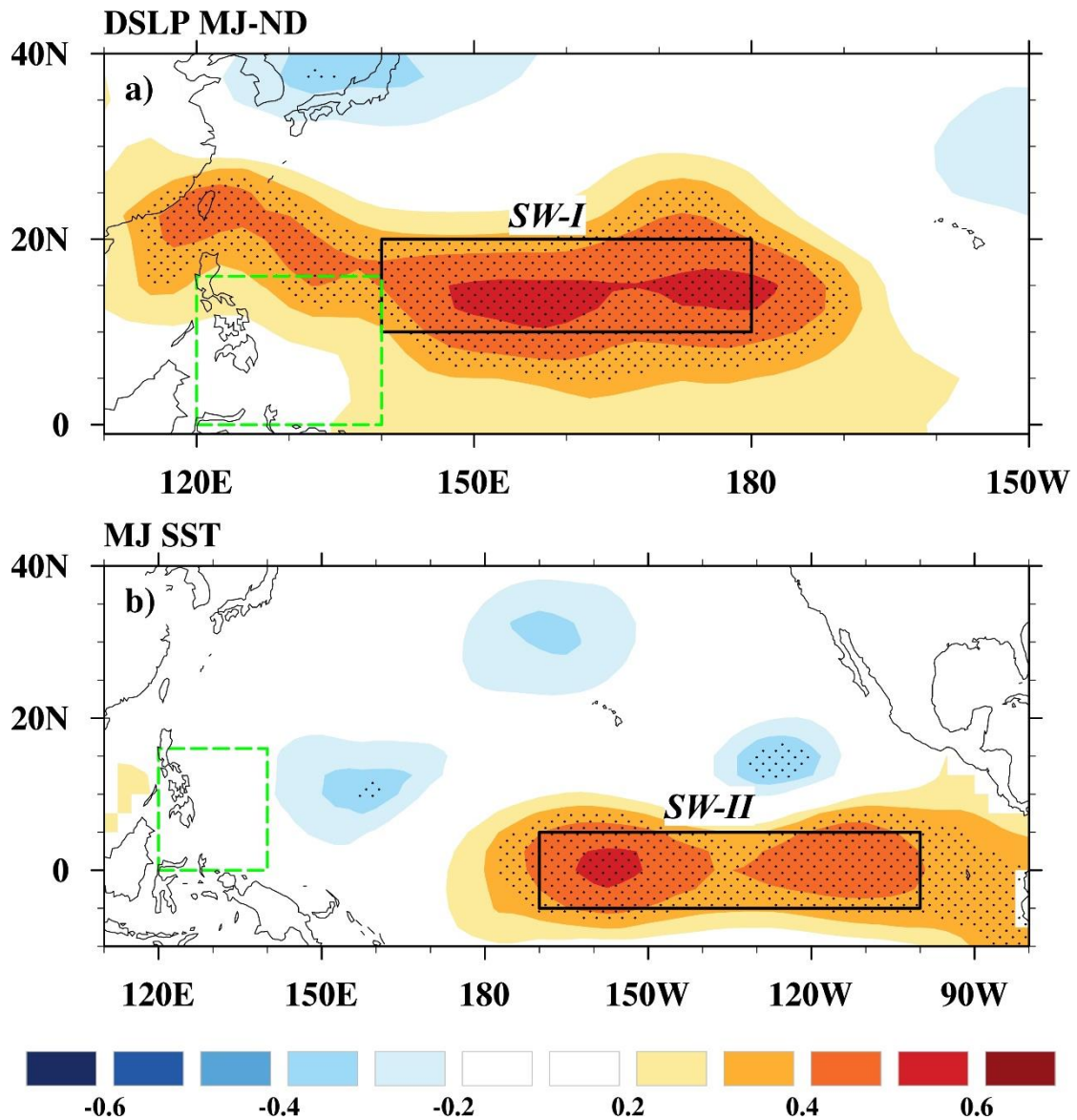


Figure 13 Predictors for TCG frequency in the southwest WNP. Correlation map between TC genesis frequency in the southwest WNP and (a) SLP tendency from November-December to May-June (shading), and (b) May-June mean SST during 1965-2000. Dotted areas denote regions with correlation coefficients significant at 95% confidence level. The black boxes represent the location of predictors and green boxes indicate boundaries of the southwest WNP.

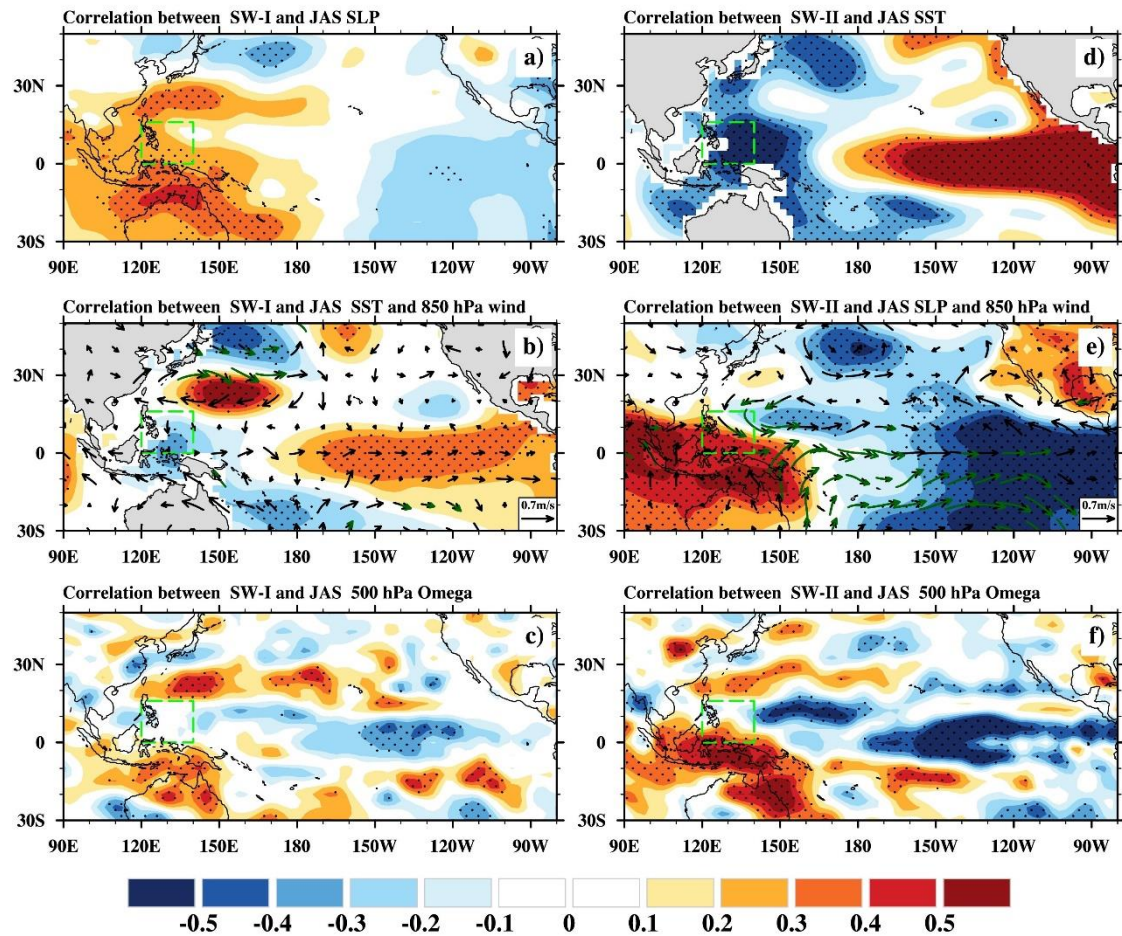


Figure 14 The lead-lag correlation between predictors for TCG in the southwest WNP and July–September mean large-scale conditions. The correlation maps between predictor SW-I and July–September mean (a) SLP (shadings), (b) SST (shadings) and 850 hPa wind (vectors), and (c) 500 hPa omega during 1965–2000. The correlation maps between predictor SW-II and July–September mean (a) SST (shadings), (b) SLP (shadings) and 850 hPa wind (vectors), and (c) 500 hPa omega during 1965–2000. The green vectors and dotted areas denote regions with correlation coefficients significant at 95% confidence level. The green boxes indicate boundaries of the southwest WNP.

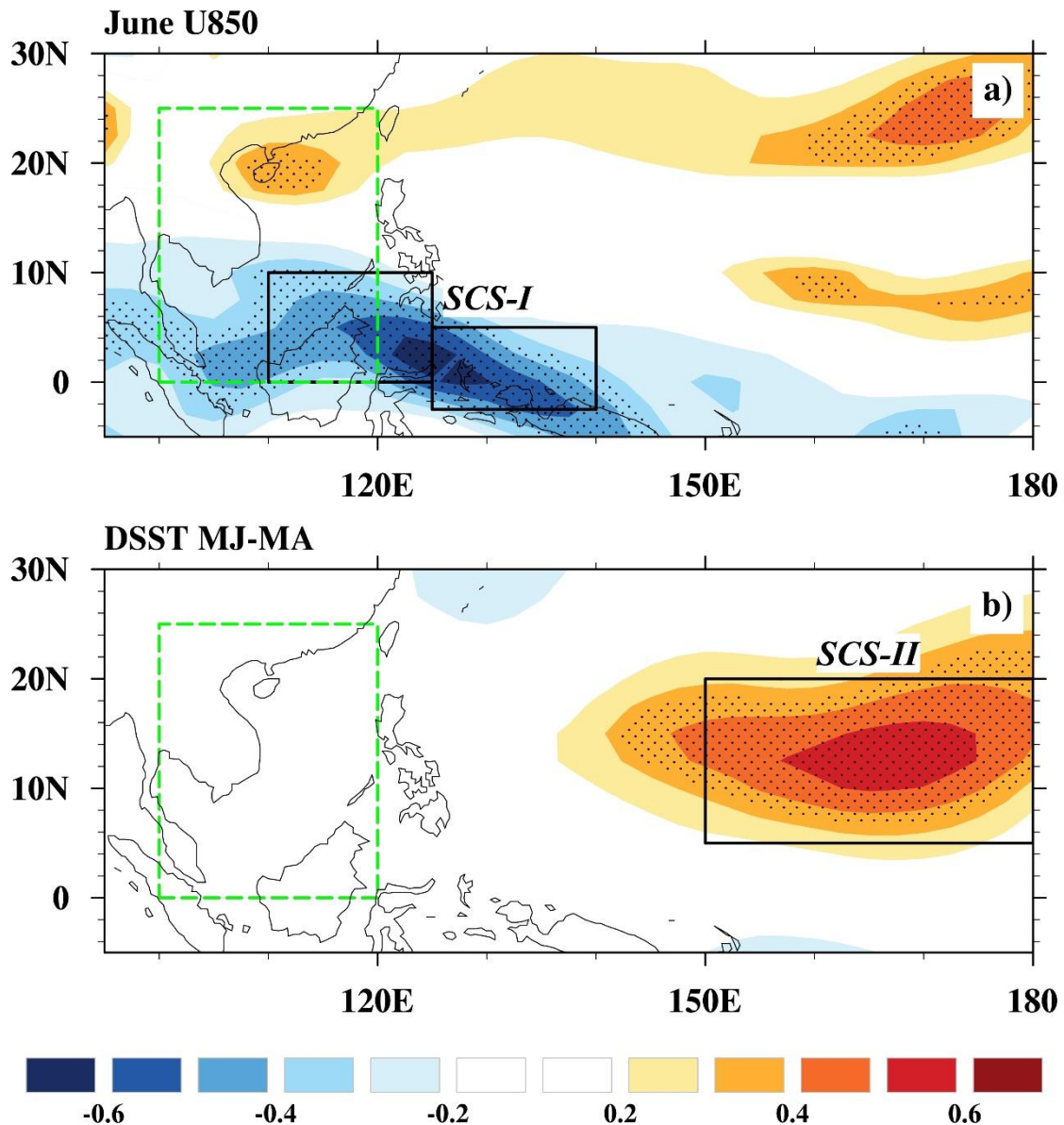


Figure 15 Predictors for TCG frequency in the South China Sea. Correlation map between TC genesis frequency in the South China Sea and (a) SLP tendency from November-December to May-June (shading), and (b) SST tendency from September-October to May-June during 1965-2000. Dotted areas denote regions with correlation coefficients significant at 95% confidence level. The black boxes represent the location of predictors and green boxes indicate boundaries of the South China Sea.



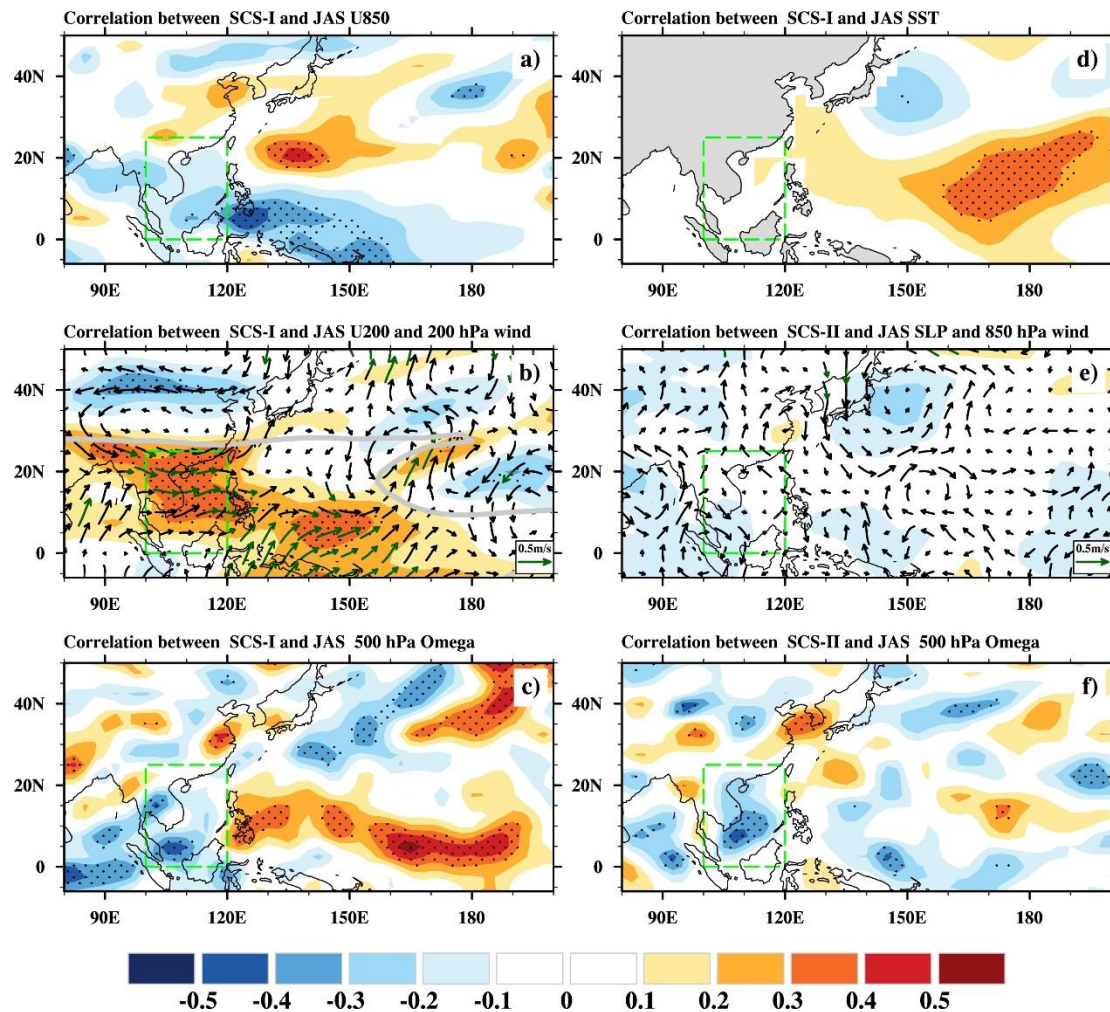


Figure 16 The lead-lag correlation between predictors for TCG in the South China Sea and July–September mean large-scale conditions. The correlation maps between predictor SCS-I and July–September mean (a) 850 hPa zonal wind (shadings), (b) 200 hPa zonal wind (shadings) and 200 hPa wind (vectors), and (c) 500 hPa omega during 1965–2000. The correlation maps between predictor SCS-II and July–September mean (d) SST (shadings), (e) SLP (shading) and 850 hPa (vectors), and (f) 500 hPa omega during 1965–2000. The grey line (b) shows the zero contour of climatological 200hPa zonal wind, which denotes the ridge of the South Asian high. The green vectors and dotted areas denote regions with correlation coefficients significant at 95% confidence level. The green boxes indicate boundaries of the South China Sea.

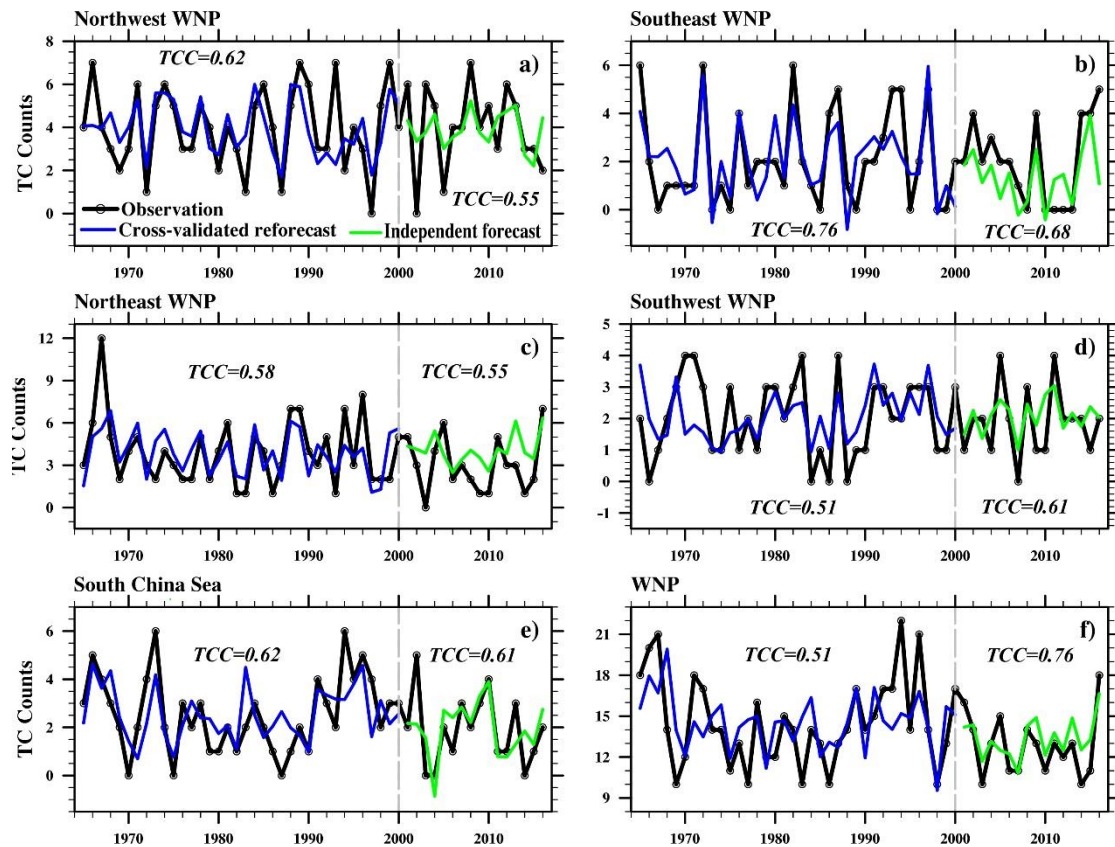


Figure 17 Predictability and prediction skill for the TCG frequency in individual sub-regions and the whole WNP. Time series of TC counts over the (a) northwest WNP (b) southeast WNP, (c) northeast WNP, (d) southwest WNP, (e) South China Sea and (f) WNP obtained from the JTWC best track (black line), cross-validated reforecast (blue line) and prediction (green line) from 1965-2016. The grey dash lines sperate the training and prediction period. The corresponding TCC is shown in each panel.

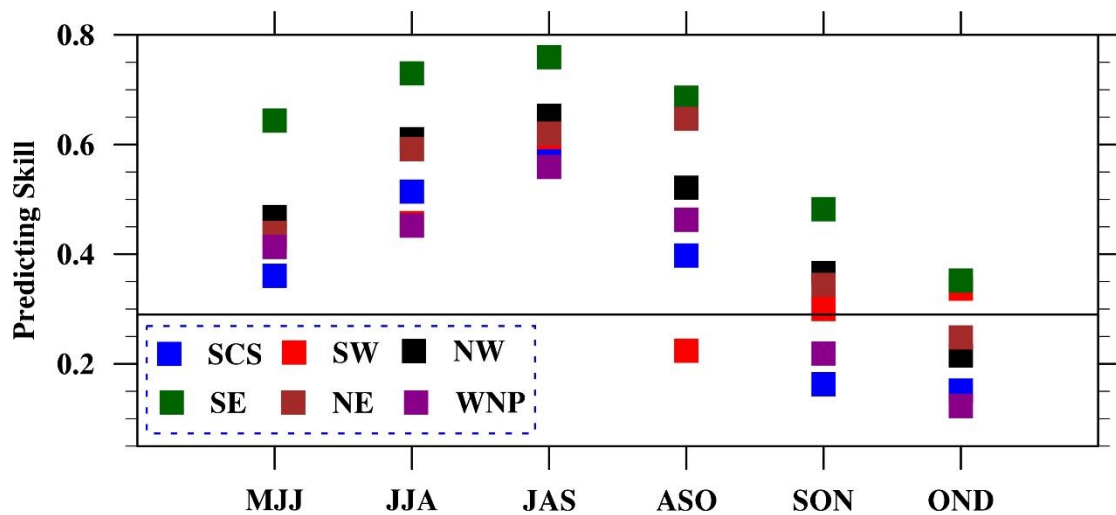


Figure 18 Correlation coefficient of predicted and observed seasonal TC genesis frequency in the SCS (blue squares), (b) southwest WNP (red squares), (c) northwest WNP (black squares), (d) southeast WNP (green squares), (e) northeast WNP (brown squares), and (f) WNP (purple squares) during 1965-2016. The black line denotes the 95% significant level.